



**UNICAMP**

**UNIVERSIDADE ESTADUAL DE CAMPINAS  
INSTITUTO DE QUÍMICA**

**NYCOLAS DOS SANTOS GALDINO**

**AVALIAÇÃO DO DESEMPENHO DE FILMES CATALÍTICO ANÓDICOS DE  
NiHCF COM VACÂNCIAS DE CIANETO E POR DECOMPOSIÇÃO TÉRMICA**

**EVALUATION OF ELECTROCATALYTIC PERFORMANCE OF THE NiHCF  
CATALYTIC ANODIC FILMS WITH CYANIDE VACANCIES AND WITH HEAT  
TREATMENT**

**CAMPINAS  
2024**

**NYCOLAS DOS SANTOS GALDINO**

**AVALIAÇÃO DO DESEMPENHO DE FILMES CATALÍTICO ANÓDICOS DE NiHCF  
COM VACÂNCIAS DE CIANETO E POR DECOMPOSIÇÃO TÉRMICA**

**EVALUATION OF ELECTROCATALYTIC PERFORMANCE OF THE NiHCF  
CATALYTIC ANODIC FILMS WITH CYANIDE VACANCIES AND WITH HEAT  
TREATMENT**

Dissertação de Mestrado apresentada ao Instituto de Química da Universidade Estadual de Campinas como parte dos requisitos exigidos para a obtenção do título de Mestre em Química na área de Química Inorgânica.

Master's Dissertation presented to the Institute of Chemistry of the University of Campinas as part of the requirements to obtain the title of Mater in Chemistry in the area of Inorganic Chemistry.

**Orientador: Prof. Dr. Juliano Alves Bonacin**

O arquivo digital corresponde à versão final da Dissertação defendida pelo aluno **Nycolas dos Santos Galdino** e orientada pelo **Prof. Dr. Juliano Alves Bonacin**.

Ficha catalográfica  
Universidade Estadual de Campinas (UNICAMP)  
Biblioteca do Instituto de Química  
Simone Luiz Alves - CRB 8/9094

G131e Galdino, Nycolas dos Santos, 1999-  
Evaluation of electrocatalytic performance of the NiHCF catalytic anodic films with cyanide vacancies and with heat treatment / Nycolas dos Santos Galdino. – Campinas, SP : [s.n.], 2024.

Orientador: Juliano Alves Bonacin.  
Dissertação (mestrado) – Universidade Estadual de Campinas (UNICAMP), Instituto de Química.

1. Vacâncias. 2. Tratamento térmico. 3. Hexacianoferrato de níquel. 4. Oxidação. 5. Engenharia de defeitos. I. Bonacin, Juliano Alves, 1980-. II. Universidade Estadual de Campinas (UNICAMP). Instituto de Química. III. Título.

Informações Complementares

**Título em outro idioma:** Avaliação do desempenho de filmes catalítico anódicos de NiHCF com vacâncias de cianeto e por decomposição térmica

**Palavras-chave em inglês:**

Vacancies

Thermic treatment

Nickel hexacyanoferrate

Oxidation

Defect engineering

**Área de concentração:** Química Inorgânica

**Titulação:** Mestre em Química na área de Química Inorgânica

**Banca examinadora:**

Juliano Alves Bonacin [Orientador]

Kalil Cristhian Figueiredo Toledo

William Reis de Araujo

**Data de defesa:** 01-08-2024

**Programa de Pós-Graduação:** Química

**Identificação e informações acadêmicas do(a) aluno(a)**

- ORCID do autor: <https://orcid.org/0009-0003-7467-1552>

- Currículo Lattes do autor: <http://lattes.cnpq.br/4990666839050559>

## BANCA EXAMINADORA

Prof. Dr. Juliano Alves Bonacin (Orientador)

Prof. Dr. William Reis de Araujo (UNICAMP)

Prof. Dr. Kalil Cristhian Figueiredo Toledo (USP)

A Ata da defesa assinada pelos membros da Comissão Examinadora, consta no SIGA/Sistema de Fluxo de Dissertação/Tese e na Secretaria do Programa da Unidade.

Este exemplar corresponde à redação final da Dissertação de Mestrado defendida pelo aluno **Nycolas dos Santos Galdino**, aprovada pela comissão Julgadora em 01 de ago. de 2024.

*Dedico este trabalho a Deus por me dar  
forças e determinação para seguir em frente.*

## **AGRADECIMENTOS**

O presente trabalho foi realizado com apoio do Conselho Nacional de Desenvolvimento Científico e Tecnológico – Brasil, (CNPq) – Código de Financiamento 131702/2022-0 e a Coordenação de Aperfeiçoamento de Pessoal de Nível Superior (CAPES) – Código 001.

Aos demais órgãos de fomento por fornecer os insumos necessários para possibilitar a pesquisa na Universidade Estadual de Campinas em Química Inorgânica e de materiais no Instituto de Química (IQ): Fundo de Amparo à Pesquisa do Estado de São Paulo (FAPESP) – Código 2021/05976-2, Coordenação de Aperfeiçoamento de Pessoal de Nível Superior (CAPES), Fundo de Apoio ao Ensino, Pesquisa e Extensão (FAEPEX) e ao Fundo de Desenvolvimento da Unicamp (FUNCAMP)

Ao Prof. Dr. Juliano Alves Bonacin pela orientação, confiança e companherismo durante toda a trajetória do meu mestrado. Foi essencial ter sido orientado pelo professor pelo alto impacto em mim no quesito de formação pessoal e profissional. Muito obrigado de coração.

Aos Prof. Dr. Jackson Dirceu Megiatto Jr., Prof. Dr. Paulo Cesar de Sousa Filho, Prof. Dr. William Reis de Araujo e Prof. Dr. Lauro Tatsuo Kubota pela formação acadêmica nas disciplinas QP157, QP212 e QP242 oferecidas pelo instituto.

Aos Prof. Dr. Pedro Paulo Corbi pela oportunidade de trabalhar como PED na disciplina Q1543, esta experiência foi essencial para a minha carreira a docência.

Aos Prof. Dr. William Reis de Araujo e Prof. Dr. Pablo Sebastián Fernández pelas contribuições para o trabalho durante o exame de qualificação de mestrado.

A técnica de laboratório Acácia Adriana Salomão pela ajuda técnica profissional e pessoal durante estes dois anos de mestrando. Muito obrigado pela sua companhia.

Aos colegas integrantes do Bonacin Research Group Evandro, Fiorella, Gabriel, João Pedro, João Marco, Luís Gustavo, Mariana, Mateus, Isabelle, Nishta, Arthur, Aline, Rogério, Rafael Kaian e aos alunos do PIBIC-EM e ex-integrantes do grupo de pesquisa Rafael, Pedro, Luiz, Theodora e Vanielle pelo apoio emocional e profissional. Vocês são incríveis e me impulsinavam sempre para não desistir. Muito obrigado por todos os momentos com todos vocês.

Aos colegas e vizinhos de laboratórios e integrantes dos Grupos de pesquisa dos professores, Prof. Dr. Pedro Paulo Corbi, Prof Dr. André Luiz Barboza Formiga e Prof. Dr. Diego Pereira dos Santos pela companhia e os momentos de comemorações que passamos juntos.

Ao corpo técnico da UNICAMP-IQ responsáveis pelos laboratório de equipamento multiusuário pelo auxílio das técnicas e conhecimento dos equipamentos utilizados.

Aos meus queridos amigos Ana, Guilherme, João Marco, João Adami, Guida pela ajuda pessoal para me dar forças e determinação para continuar com meus sonhos.

A minha amada família composta pelo meu pai Carlos Antonio de Souza Galdino, mãe Rosanildade dos Santos Galdino, irmã Karen dos Santos Galdino e irmão Carlos Antonio de Souza Galdino Junior por serem meu porto seguro. Amo vocês de coração.

*“Você nunca deve ceder ao desespero. Se permitir escorregar por  
essa estrada é se entregar aos seus instintos mais baixos.  
Nos momentos mais sombrios, a esperança é algo que você  
dá a si mesmo. Esse é o significado da força interior.”*

The Legend of Korra.

## RESUMO

A utilização de fonte energética advinda de combustível fóssil durante centenas de anos, estão diretamente relacionadas com o aumento excessivo de gás carbono emitido na Terra o que acarreta diversos efeitos climáticos adversos como o aumento anormal da temperatura do globo, prejudicando as futuras gerações. Diante deste cenário, vem se impulsionando a substituição desta matriz energética por fontes renováveis e eficientes que sejam mais amigáveis ecologicamente, com isto que a utilização do gás hidrogênio produzido por processos de eletrólise da água como opção emergente de substituir tais fontes a base de combustível fóssil se tornaram bastante atrativas, vista suas vantagens de baixo nível de emissão de gás carbônico da e com um alta eficiência energética. Apesar disso, existem uma série de limitações de produzir hidrogênio a partir do processo de eletrólise da água, visto que a etapa limitante deste processo é a reação de evolução de oxigênio que ocorre no anodo da célula eletroquímica que ocorre a oxidação da água. Isto pois é uma reação termodinamicamente desfavorável e endegônica, necessitando assim um catalisador. Neste projeto, buscou-se desenvolver catalisadores anódicos para a reação de oxidação da água a base de níquel hexacianoferratos (NiHCF) com a inserção de engenharia de defeitos em sua estrutura (NiHCF-vac) bem como por tratamentos térmicos (NiFeOx), no qual foram avaliados sua performance e desempenho eletrocatalítico para a reação de oxidação água. Os resultados demonstram um melhora catalítica a respeito da transferência de carga ( $R_{ct}$ ) de 234  $\Omega$  para 63,6  $\Omega$  e 18,9  $\Omega$ , diminuição do valor do sobrepotencial ( $\eta$ ) de 821 mV para 774 mV e 740 mV para o NiHCF, NiHCF-vac e NiFeOx, respectivamente. Os estudos com luz síncrotron a base de XPS e XAS trazem mais informações sobre as vacâncias e sua influência no desempenho catalítico. Os resultados obtidos para a reação de oxidação da água em condições neutras de reação no qual foi comparadas com outros catalisadores reportados da literatura.

## ABSTRACT

The use of the recommended energy source of fossil fuel for hundreds of years is directly linked to the excessive increase in carbon gas emitted on Earth, which leads to several adverse climate effects such as the abnormal increase in the temperature of the globe, harming future generations. Given this scenario, the replacement of this energy matrix with renewable and efficient sources that are more ecologically friendly has been promoted, with this being the use of hydrogen gas produced by water electrolysis processes as an emerging option to replace such sources. based on fossil fuels have become very attractive, given their advantages of low levels of carbon dioxide emissions and high energy efficiency. Despite this, there are a series of limitations to the production of hydrogen from the water electrolysis process, since the limiting stage of this process is an occurrence of oxygen evolution that occurs at the anode of the electrochemical cell that occurs during water oxidation. This is because it is a thermodynamically unfavorable and endergonic occurrence, thus requiring an event. In this project, we sought to develop anodic explanations for the occurrence of water oxidation based on nickel hexacyanoferrates (NiHCF) with the insertion of defect engineering in its structure (NiHCF-vac) as well as thermal treatments (NiFeOx), in which its performance and electrocatalytic performance were evaluated for the occurrence of water oxidation. The results demonstrate a catalytic improvement in charge transfer ( $R_{ct}$ ) from 234  $\Omega$  to 63.6  $\Omega$  and 18.9  $\Omega$ , a decrease in the overpotential ( $\eta$ ) from 821 mV to 774 mV and 740 mV for NiHCF, NiHCF-vac, and NiFeOx, respectively. Synchrotron light studies based on XPS and XAS provide further information about the vacancies and their influence on catalytic performance. The results obtained for the water oxidation reaction under neutral conditions were compared with other catalysts reported in the literature.

## LISTA DE ILUSTRAÇÕES

Figure 1: CO<sub>2</sub> emission by fuel industry (A) and the temperature anomaly (B) over 1850 – 2022 Global data. (source: <https://ourworldindata.org/>);

Figure 2: Color classification of H<sub>2</sub> production processes to environmental criteria (extracted from Von Zobel *et al.*);

Figure 3: Comparison of different hydrogen production technologies from water. (Megía, *et al.*);

Figure 4: Pourbaix diagram for water electrolysis (R. Sharifian *et al.* – modified);

Figure 5: Green H<sub>2</sub> by water splitting iceberg scheme (created by author);

Figure 6: Abundance, atoms of elements per atoms of Si in the Earth;

Figure 7: Prussian Blue cubic coordination network structure scheme. A<sub>n</sub>M<sub>x</sub>[M'(CN)<sub>6</sub>]-H<sub>2</sub>O, where A is an alkali metal ion (purple), and M (light grey) and M'(gold) are transition metal ions;

Figure 8: Schematic ways to create defects in nanomaterials (L. Lei *et al.*);

Figure 9: Versatility of using Prussian Blue and analogues as *template* precursor. (Bornamehr, *et al.*);

Figure 10: Chronoamperograms obtained for Ni<sup>0</sup> (A), NiHCF (B) and NiHCF-vac (C) electrodeposition synthesis as pale-grey, black and green line, respectively;

Figure 11: Catalytic cycle mechanism pathways proposed by the OER. (Craig, M. *et al.*);

Figure 12: Electronic spectroscopy UV-visible absorbance study of NiHCF (A) and NiHCF-vac (B) films in black and green line, respectively;

Figure 13: Vibrational Raman spectroscopy for NiHCF and NiHCF-vac in black and green solid lines respectively;

Figure 14: Vibrational Raman spectroscopy comparison to NiHCF to NiFeOx spectra;

Figure 15: Morphological studies structures in NiHCF and NiHCF-vac, using scanning electron microscopy;

Figure 16: Scanning electron microscopy (SEM) and mapping elements of C, Fe, N and Ni by EDS for NiHCF and NiHCF-vac in 5  $\mu\text{m}$ ;

Figure 17: Atomic force microscopy topography image. FTO glass substrate (A), NiHCF (B) and NiHCF-vac, respectively;

Figure 18: Atomic force microscopy 3D topography image. Left to right. FTO glass substrate, NiHCF and NiHCF, respectively;

Figure 19: Atomic force microscopy topography image for NiHCF after heat treatment. NiFeO<sub>x</sub> and NiFeO<sub>x-vac</sub>;

Figure 20: Atomic force microscopy 3D topograph imagens comparison from NiHCFs to NiFeO<sub>x</sub>;

Figure 21: Cyclic voltammogram for NiHCFs in 0.5 M KNO<sub>3</sub> pH 7.29 condition. NiHCF and NiHCF-vac in black and green line, respectively;

Figure 22: Adapted Randle's circuit for fitting simulation for EIS results;

Figure 23: Electrochemical impedance spectroscopy Nyquist plot for FTO glass substrate, NiHCF and NiHCF-vac in pale-grey, black and green line (A) and comparison from NiHCF to NiFeO<sub>x</sub> in blue line (B), respectively at 2.31 V E vs. RHE (1.7 V E<sub>Ag/AgCl</sub>), from 5.10<sup>5</sup>Hz to 0,005 Hz;

Figure 24: Left to right. Linear sweep voltammetry for FTO glass substrate, NiHCF, NiHCF-vac, NiFeO<sub>x</sub> and NiFeO<sub>x-vac</sub> in pale-grey, black, green, blue and pink line, respectively at scan rate 5 mVs<sup>-1</sup>;

Figure 25: Tafel plot for NiHCF, NiHCF-vac, NiFeO<sub>x</sub>, NiFeO<sub>x-vac</sub> and RuO<sub>2</sub> in black, green, blue, pink and cyan line, respectively;

Figure 26: Soft X-ray photoelectron spectra of FTO glass, NiHCF and NiHCF-vac in pale-grey, black and green line (A). FTO glass, NiFeO<sub>x</sub> and NiFeO<sub>x-vac</sub> in pale-grey, blue and pink line (B);

Figure 27: Soft X-ray absorption spectra for Fe and Ni L<sub>3,2</sub> edges in NiHCF and NiHCF-vac before and after catalysts under mild conditions. Total electron yield (TEY) surface analysis and fluorescent yield (FY) bulk analysis;

Figure 28: Soft X-ray absorption spectra for Fe and Ni L<sub>3,2</sub> edges in NiHCF and NiFeOx before the catalysts under mild conditions. Total electron yield (TEY) surface analysis and fluorescent yield (FY) bulk analysis;

S1: Schematic Raman spectroscopy *in situ* study using a screen-printed carbon electrode in a droplet electrolyte;

S2: Schematic electronic UV-visible spectroscopy *in situ* study using a miniaturized electrochemical cell as a cuvette;

S3: Schematic oxygen quantification chamber during the electrocatalysis using a polarography dissolved oxygen sensor, and their respective quantification values using different working electrodes.

S4: UV-visible electronic absorbance spectra of NiCl<sub>6</sub>·H<sub>2</sub>O, Ferricyanide, Ferrocyanide, Prussian Blue, Berlin green, NiHCF(using ferrocyanide) and NiHCF(using ferricyanide), respectively.

S5: Raman spectroscopy of RuO<sub>2</sub> produced for catalysis comparison. The three peaks, are vibrational modes characteristics for RuO<sub>2</sub>.

S6: Soft X-ray photoelectron spectroscopy survey in 150 – 0 eV for NiHCF, NiHCF-vac, NiFeOx and NiFeOx-vac, in black, green, blue and pink lines, respectively. All these materials have slight differences in Ni 3s (111.0 eV) , Fe 3s (91.3 eV), Ni 3p (67.5 – 66 eV) and Fe 3p (57.7 eV). Other peaks are assigned for FTO glass substrate.

## LISTA DE TABELAS

Table 1: Daily metal prices in dollars per oz. (Source: <https://www.dailymetalprice.com/>);

Table 2: Electronic absorbance UV-Vis band and their respectively assignment for NiHCF and NiHCF-vac and the comparison with PB, BG and their respectively precursors;

Table 3: Raman vibrational modes assignment for NiHCF and NiHCF-vac materials;

Table 4: Electrochemical results obtained using electrochemical impedance spectroscopy. To calculate ECSA value, we use  $Q_{DL}$  divided by the  $C_s$  as  $35 \mu F \cdot cm^{-2}$ ;

Table 5: Electrocatalysts parameters obtained and comparison with Prussian Blue (PB) and RuO<sub>2</sub> for anodic catalysts for water electrolysis under mild conditions. \*The PB use a different method to calculate ECSA;

Table 6: Atomic composition (At %) of Ni, Fe, N, and C elements in NiHCF and NiHCF-vac samples.

Table 7: Surface analysis (TEY) before and after catalysis differences in Ni and Fe L<sub>3,2</sub> edges in NiHCF, NiHCF-vac and NiFeOx.

# SUMÁRIO

<b>1. INTRODUCTION</b>	<b>17</b>
1.1 ENERGETIC SCENARIO: A BRIEF REVIEW	17
1.2 HYDROGEN GAS A POTENTIAL OPTION AS ENERGY RENEWABLE SOURCE	17
1.3 CHALLENGES TO PRODUCE H <sub>2</sub> BY WATER ELECTROLYSIS	19
1.5 PRUSSIAN-BLUE AND ITS ANALOGUES AS AN EARTH-ABUNDANT ANODIC CATALYST	22
1.6 DEFECTS ENGINEERING: A WAY TO IMPROVE THE CATALYTIC PERFORMANCE	23
1.7 PRUSSIAN-BLUE AS <i>TEMPLATE</i> TO PRODUCE MIXED OXIDES CATALYST	24
<b>2. OBJECTIVES</b>	<b>26</b>
<b>3. EXPERIMENTAL PROCEDURES</b>	<b>27</b>
3.1 REAGENTS AND MATERIALS	27
3.2 SUBSTRATE PREPARATION	27
3.3 ANODIC CATALYST FILMS PREPARATION PROCESS	27
3.3.1 <i>Metallic nickel film deposition</i>	27
3.3.2 <i>Nickel Prussian blue analogues film synthesis (NiHCF)</i>	28
3.3.3 <i>Nickel Prussian blue analogues with cyanide vacancies film synthesis (NiHCF-vac)</i>	28
3.3.4 <i>Nickel-Iron mixed oxides film synthesis (NiFeO<sub>x</sub>)</i>	28
3.3.5 <i>RuO<sub>2</sub> preparation film synthesis</i>	28
3.4 SPECTROSCOPY CHARACTERIZATION TECHNIQUES	28
3.4.1 <i>Electronic UV-Visible absorbance spectroscopy</i>	28
3.4.2 <i>Vibrational Raman spectroscopy</i>	28
3.5 MICROSCOPY CHARACTERIZATION TECHNIQUES	29
3.5.1 <i>Scanning electron microscopy</i>	29
3.5.2 <i>Atomic force microscopy</i>	29
3.6 ELECTROCHEMICAL CHARACTERIZATION	29
3.6.1 <i>Cyclic voltammetry</i>	29
3.6.2 <i>Linear sweep voltammetry</i>	29
3.6.3 <i>Electrochemical impedance spectroscopy</i>	30
3.6.4 <i>Electrocatalytic evaluation tests</i>	30
3.7 SOFT X-RAY SPECTROSCOPY CHARACTERIZATION	30
3.7.1 <i>X-ray Photoelectron spectroscopy</i>	30
3.7.2 <i>X-ray Absorption spectroscopy</i>	31
3.8 SUPPLEMENTARY MEASURES	31
<b>4. RESULTS AND DISCUSSION</b>	<b>32</b>
4.1 ANODIC CATALYST FILM SYNTHESIS	32
4.1.1 <i>NiHCF</i>	32
4.1.2 <i>NiFeO<sub>x</sub></i>	33
4.1.3 <i>RuO<sub>2</sub></i>	34

4.2 ELECTRONIC UV-VISIBLE ABSORBANCE SPECTROSCOPY .....	34
4.3 VIBRATIONAL RAMAN SPECTROSCOPY .....	35
4.4 MICROSCOPY CHARACTERIZATION.....	37
4.4.1 <i>Scanning electronic microscopy</i> .....	37
4.4.2 <i>Atomic force microscopy</i> .....	39
4.5 ELECTROCHEMICAL STUDIES .....	42
4.5.1 <i>Cyclic voltammetry</i> .....	42
4.5.2 <i>Electrochemical impedance spectroscopy</i> .....	43
4.5.3 <i>Linear sweep voltammetry</i> .....	46
4.6 ELECTROCATALYSIS EVALUATION PARAMETERS .....	47
4.7 SOFT X-RAY SPECTROSCOPY CHARACTERIZATION.....	48
4.7.1 <i>X-ray photoelectron spectroscopy</i> .....	48
4.7.2 <i>X-ray absorbance spectroscopy</i> .....	50
<b>5. CONCLUSION.....</b>	<b>54</b>
<b>REFERENCES .....</b>	<b>55</b>
<b>APPENDIX .....</b>	<b>60</b>

## 1. INTRODUCTION

### 1.1 Energetic scenario: a brief review

It is well-known that global problems have arisen over the centuries with the excessive use of fossil fuels as the world's main energy source, causing *quasi-irreversible* worldwide environmental damage, the effects of greenhouse gases, severe climatic changes and events, and pollution. These are some issues that geopolitical and economic actions must address. Recent data listed by the *Our World in Data* website associate the snowball temperature effect with the increase in carbon dioxide (CO<sub>2</sub>) emission from industrial fuel worldwide, and we can observe clear relationship between the growth in energy demand (Figure 1A) and greenhouse gases emissions. As a result, the world temperature has increased significantly (Figure 1B)<sup>1</sup>.

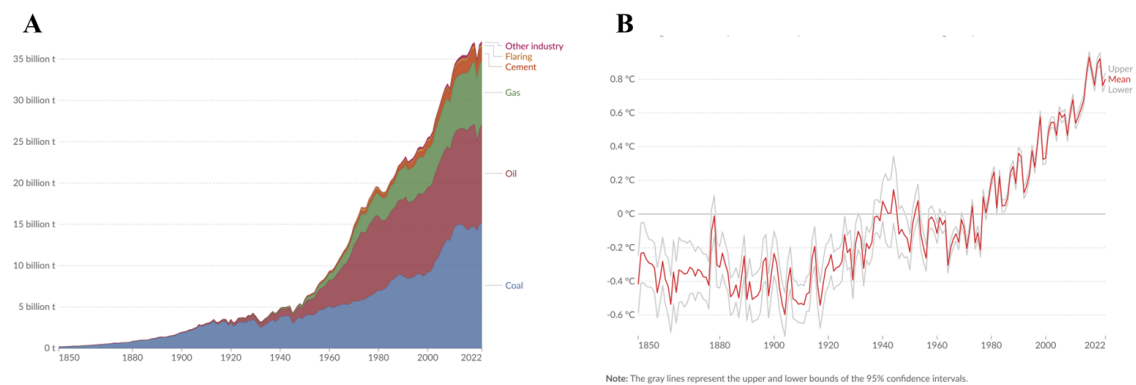


**Figure 1:** CO<sub>2</sub> emission by fuel industry (A) and the temperature anomaly (B) over 1850 – 2022 Global data. (source: <https://ourworldindata.org/>)

Transition to renewable energy sources is crucial to mitigate these impacts and guarantee a sustainable future for the next generations. One of the possible sources being produced and tested at an industrial scale is hydrogen gas (H<sub>2</sub>) as a clean energy source<sup>2,3</sup>.

### 1.2 Hydrogen gas a potential option as energy renewable source

Hydrogen gas (H<sub>2</sub>) is an important raw material produced and applied in various industrial sectors such as petrochemicals, fertilizers, and energy. Their demand production is essential for some materials, such as ammonia (NH<sub>3</sub>), methanol (CH<sub>4</sub>) and stainless steel<sup>2</sup>. Because of its relevance in industry hydrogen is produced. The H<sub>2</sub> production process is related to some criteria such as CO<sub>2</sub> emission, environmental impacts and the level of cleanliness of the obtained H<sub>2</sub> in the process, which can be indicated by a hydrogen color code (Figure 2). H<sub>2</sub> produced from fossil fuels has a high

CO<sub>2</sub> emission, high environmental impact, and is considered *dirty*, namely brown, gray and/or blue hydrogen. However, it is possible to produce hydrogen that emits low levels of CO<sub>2</sub> emission with low environmental damage and *cleanliness* level of the hydrogen derived from alternative sources or through electrolysis, like green hydrogen.

Color Code	Process	CO <sub>2</sub> Emission	Environmental Impact	Cleanliness Level of the H <sub>2</sub>
Fossil Fuels	H <sub>2</sub> Coal → H <sub>2</sub> ; Gasification process, syngas, T=700°C. CO <sub>2</sub> emitted directly			
	H <sub>2</sub> Natural gas (CH <sub>4</sub> ) → H <sub>2</sub> ; Steam Reforming. Most common process			
	H <sub>2</sub> Natural gas (CH <sub>4</sub> ) → H <sub>2</sub> ; Steam reforming with capture and store of CO <sub>2</sub>			
	H <sub>2</sub> Natural gas (CH <sub>4</sub> ) → H <sub>2</sub> ; Methane pyrolysis with production of solid carbon			
Electrolysis	H <sub>2</sub> H <sub>2</sub> production from water electrolysis through nuclear energy			
	H <sub>2</sub> H <sub>2</sub> production from water electrolysis through mixture of sources (FF and RE)			
	H <sub>2</sub> H <sub>2</sub> production from water electrolysis through renewables sources			
Alternative	H <sub>2</sub> Natural occurrence, rare on Earth. H <sub>2</sub> is found in clathrates or in the atmosphere (1 ppm)			
	H <sub>2</sub> Thermochemical water splitting produced by concentrated solar energy			
	H <sub>2</sub> H <sub>2</sub> produced from garbage, plastic or biomass			

low    medium    large

**Figure 2:** Color classification of H<sub>2</sub> production processes to environmental criteria (extracted from Von Zubeil *et al.*).

Although hydrogen produced by water electrolysis processes has high energy efficiency and yield, its production cost is high (Figure 3)<sup>4</sup>, making it impossible to compete with cheaper and more consolidated energy sources derived from fossil fuels. In this way, most of the hydrogen produced is classified as gray and blue (around 95%), and only 5% of hydrogen comes from renewable energy sources such as *water splitting* (green hydrogen)<sup>2,3</sup>. It is necessary to understand some obstacles that result in only 5% of hydrogen coming from renewable sources.

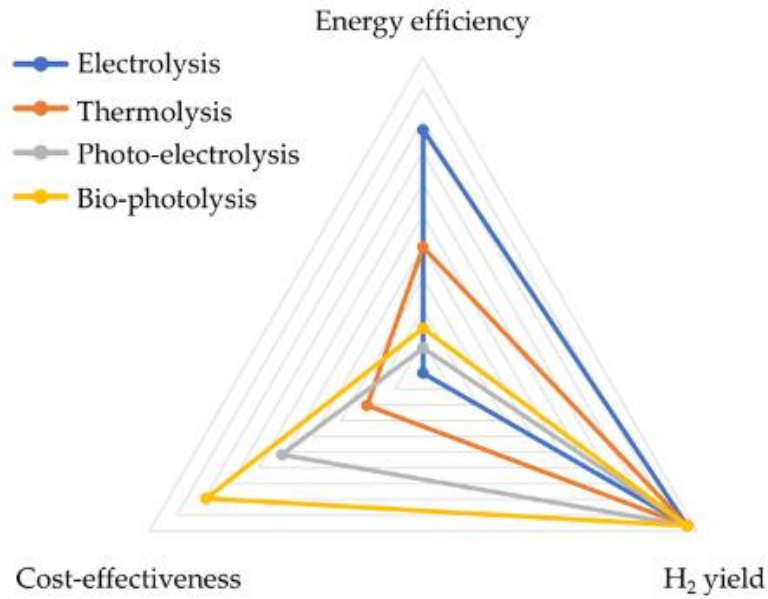


**Figure 3:** Comparison of different hydrogen production technologies from water. (Megía, *et al.*)

### 1.3 Challenges to produce H<sub>2</sub> by water electrolysis

Water splitting is the overall reaction, which can be divided into two half-reactions: the hydrogen evolution reaction (HER) (1) and the oxygen evolution reaction (OER) (2), and their conditions are demonstrated below. As we can observe, the water electrolysis reaction in an electrochemical cell, is a thermodynamically unfavorable process ( $\Delta G > 0$ ) and has a standard potential ( $E^0$ ) of 1.23 V to initiate the electrochemical reaction, and this value is independent of the cell's pH conditions (Figure 4)<sup>5</sup>. The OER semi-reaction is considered one of the sluggish factors in water electrolysis since oxidized water to produce gas oxygen (O<sub>2</sub>) requires four electrons, which results in a standard potential of 1.23 V. Therefore, it is necessary to use anodic catalysts to reduce the thermodynamic barrier of the water splitting reaction overall (3)<sup>6-8</sup>.



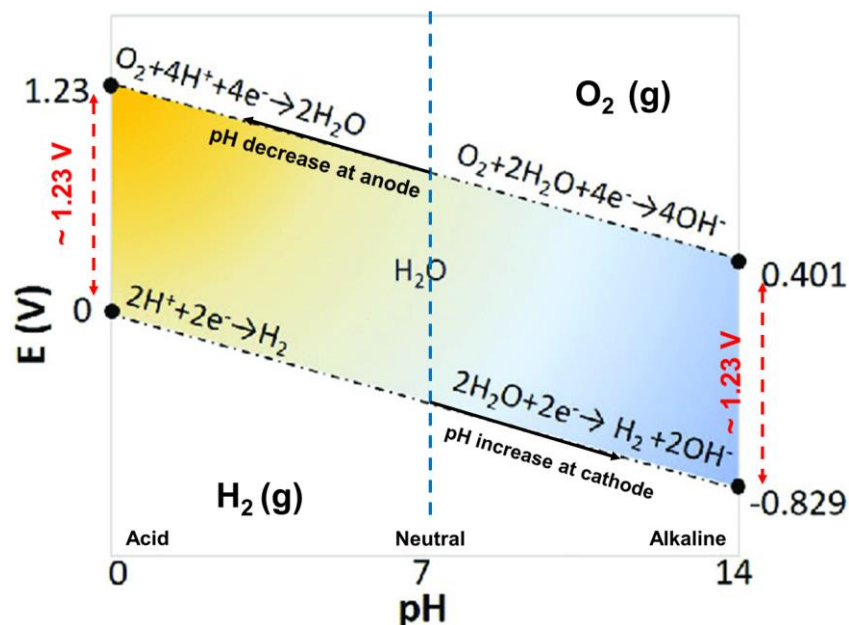


**Figure 4:** Pourbaix diagram for water electrolysis (R. Sharifian *et al.* – modified).

On an industrial scale, the state-of-the-art catalysts for the water splitting reaction involve the use of noble metal-based anodic catalysts such as Ir, Ru, Pt, and their oxides<sup>9,10</sup>, which is one of the factors that makes hydrogen produced by this method four times more expensive than hydrogen derived from fossil fuels. From this principle, we can understand the iceberg problem of finding catalysts for the water-splitting reaction.

The use of noble metals as anodic catalysts is just the "tip" of the iceberg in terms of the challenges of producing hydrogen through water electrolysis (Figure 5). Besides this, there are other obstacles such as the need for stable and highly efficient catalysts over long periods of use, high efficiency, and the fact that the technology used in proton exchange membrane (PEM), anion exchange membrane (AEM), and solid oxide electrolyzer cell (SOEC) electrolyzers is still under development<sup>11,12</sup>. These factors increase costs and hinder the large-scale industrial production of green hydrogen. Other challenges are deeper and more complex to discuss now, such as geopolitical issues (transportation, storage, laws, and safety) and the competitive cost and accessibility of this fuel compared to current primary energy sources.

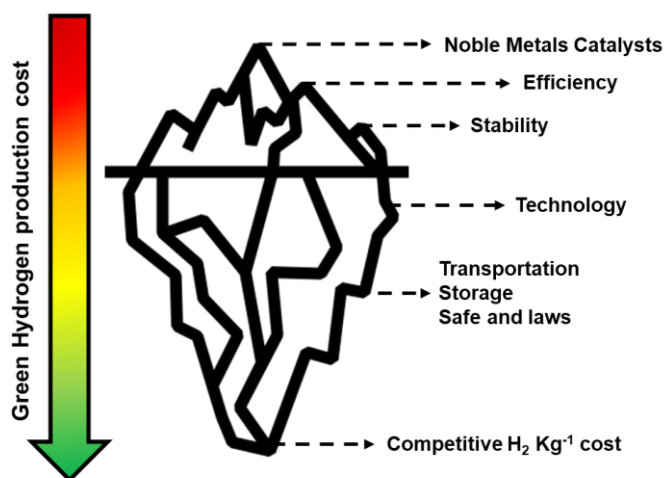


**Figure 5:** Green H<sub>2</sub> by water splitting iceberg scheme (created by author).

To overcome the initial obstacles, it is worth investigating the use of elements from the first transition series of the periodic table due to their relative earth-abundance and low cost compared to less abundant and expensive noble metal elements (Figure 6)<sup>13</sup>. Elements from the first transition series, such as Co, Ni, Cu, and Fe, offer a cheap and abundant possibility instead of noble metals (Table 1) wide range of potential catalysts for the water-splitting reaction, requiring an analysis of their stability and efficiency when using these elements.

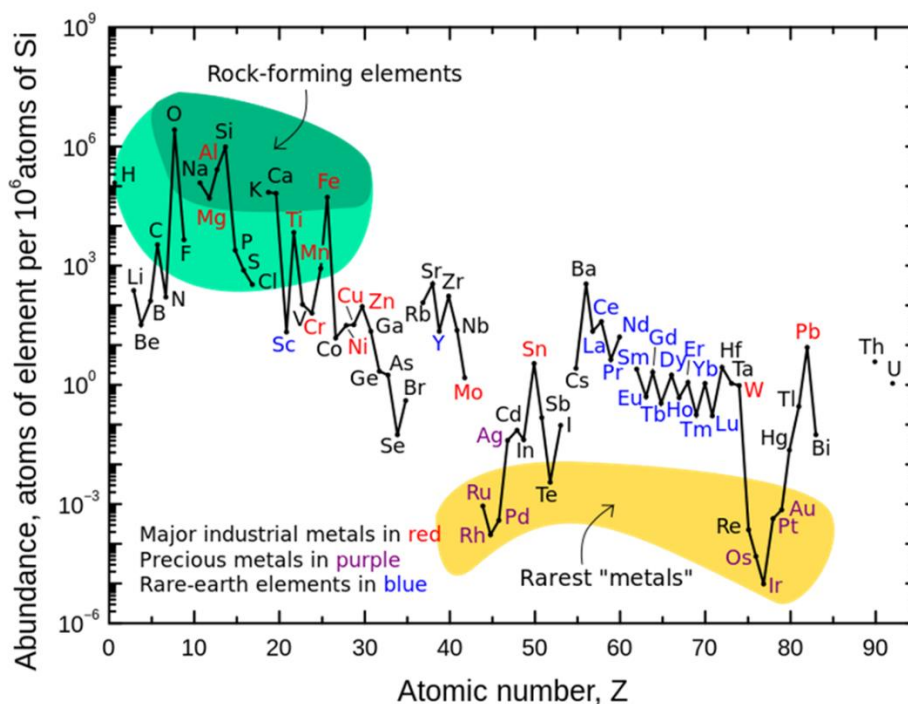


**Figure 6:** Abundance, atoms of elements per atoms of Si in the Earth.

**Table 1:** Daily metal prices in dollars per oz. (Source: <https://www.dailymetalprice.com/>).

Element	Price (US / oz)
Ir	$4.80 \times 10^3$
Rh	$4.75 \times 10^3$
Au	$2.42 \times 10^3$
Pt	$1.10 \times 10^3$
Ru	$4.30 \times 10^2$
Co	$8.65 \times 10^{-1}$
Ni	$6.70 \times 10^{-1}$
Cu	$3.51 \times 10^{-2}$
Fe <sub>(Ore)</sub>	$3.65 \times 10^{-3}$

### 1.5 Prussian-blue and its analogues as an earth-abundant anodic catalyst

The research and development of catalysts based on earth-abundant elements have given significant attention to Prussian Blue (PB) and its analogs (PBA) as catalysts for water oxidation, due to their simple production, robustness, and efficiency under mild and acidic conditions<sup>7</sup>. Prussian Blue and its analogues are part of the cyanometallate family, with a structure consisting of two coordinated metals linked by cyanide bridges, forming an organized cubic coordination network<sup>14</sup>. Their common structure is shown in Figure 7 and it can be described as  $A_nM_x[M'(CN)_6] \cdot H_2O$ , where A is an alkali metal ion (purple), and M (light grey) and M'(gold) are transition metal ions.

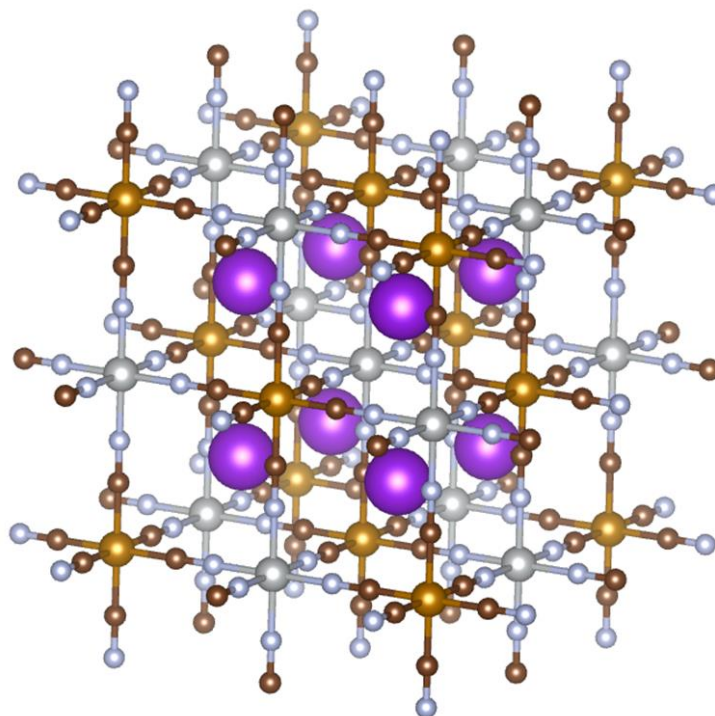


**Figure 7:** Prussian Blue cubic coordination network structure scheme.  $A_nM_x[M'(CN)_6] \cdot H_2O$ , where A is an alkali metal ion (purple), and M (light grey) and M' (gold) are transition metal ions.

Prussian blue (PB) and its analogs (PBA) are widely recognized and studied as anodic catalysts for water oxidation, demonstrating good performance under acid and neutral conditions. Despite their good stability, they present a lower concentration of active sites and charge transfer, significantly limiting their catalytic activity. Consequently, it is necessary to investigate methods that improve its catalytic performance as a catalyst for water oxidation under mild conditions. In this way, the implementation of engineering defect creation in those materials aims to enhance their catalytic performance<sup>15</sup>. This is due to the direct impact of defect development on properties such as electrical conductivity and charge transfer, leading to a greater number of active sites in the system, thereby improving the catalytic performance of the modified catalyst.

### **1.6 Defects engineering: a way to improve the catalytic performance**

In an overview, we have identified many methods for engineering defect creation in modified electrodes, categorized by the dimension of structural defects: point, line, planar, and volume defects (Figure 8)<sup>15</sup>. Furthermore, the creation of engineering defects is correlated with the synthesis process of the catalyst, implying that the catalyst production involves the introduction of defects into its structure. We have chosen the electrodeposition method to produce our catalyst, as it offers good reproducibility and

straightforward material synthesis. Moreover, there is limited research on defect creation through electrochemistry processes.

Defect creation in catalysts is well-documented in the literature, particularly the oxygen vacancy defects ( $v_o$ ) in oxide-based catalysts to enhance electrocatalytic performance. However, there are only a few known studies on the cyanide vacancy defects ( $v_{CN^-}$ ) creation in modified electrodes based on cyanometallates like Prussian blue and its analogs<sup>16-18</sup>. Furthermore, most of the cyanide defect creation methods published in the literature are highly specialized, making laboratory-scale production challenging and increasing material production costs.

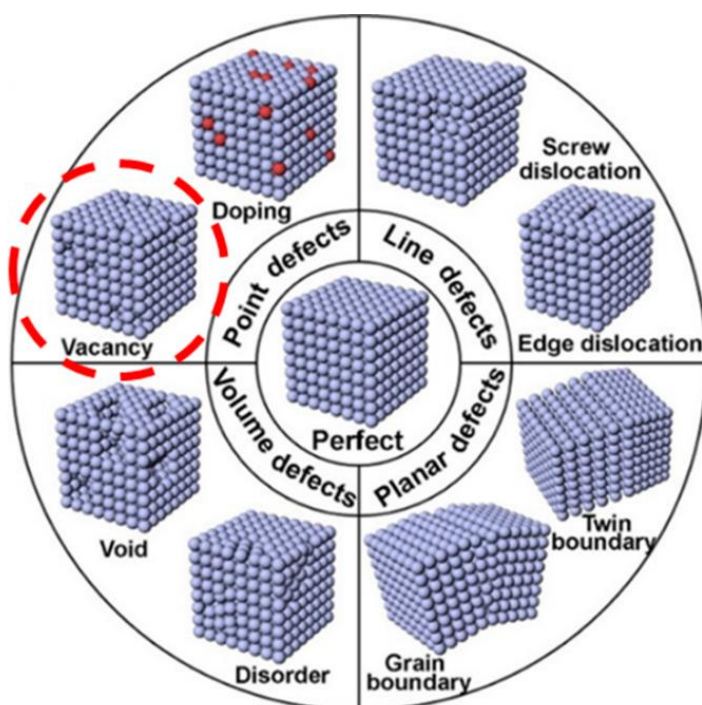


**Figure 8:** Schematic ways to create defects in nanomaterials (L. Lei *et al*).

In this way, we synthesized films of Nickel-based Prussian blue Analogues (NiHCF) through electrodeposition and developed an activation process that introduces defects into their structures (NiHCF-vac). This effort aims to enhance their electrocatalytic activity for oxygen production in the water oxidation reaction (WOR) under mild conditions (pH ~ 7).

### 1.7 Prussian-blue as *template* to produce mixed oxides catalyst

One characteristic of Prussian blue analogues is the extensively versatility to use as template precursor to generate of novel catalysts by different methodology, modifying their porosity, structure shape and size control such as oxides, carbides,

alloys or metal nanoparticles are some examples of materials that can be derived from Prussian Blue<sup>19</sup> (Figure 9). The new catalysts generated mixed oxide catalysts which is another way to improve the performance towards the water oxidation reaction. In this way, we will use the Prussian blue analogue of nickel to produce mixed nickel-iron oxides ( $\text{NiFeO}_x$ ), electrochemically and evaluate the electrocatalytic performance for OER<sup>7</sup> under mild conditions.

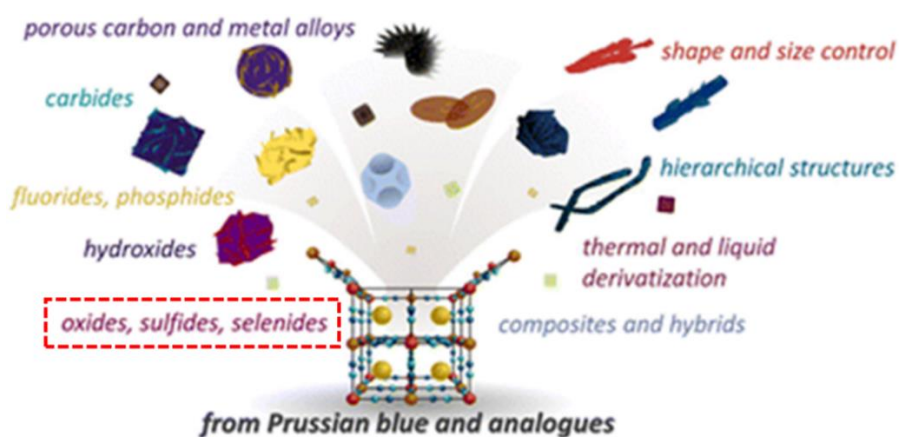


**Figure 9:** Versatility of using Prussian Blue and analogues as *template* precursor. (Bornamehr, *et al.*)

## 2. OBJECTIVES

### Main objective:

- Evaluate the electrocatalytic activity towards water oxidation in nickel Prussian blue analogues (NiHCF) and their oxides as anodic catalysts films under mild conditions.

### Specific objectives:

- Create and verify cyanide defects electrochemically in nickel Prussian blue analogues (NiHCF-vac);
- Use the analogue as a template to synthesize their oxides (NiFeO<sub>x</sub>) to increase the catalytic activity for water oxidation reaction;
- Synthesize ruthenium oxide (RuO<sub>2</sub>) to evaluate catalytic performance and compare with the previously evaluated catalysts under mild conditions.

### 3. EXPERIMENTAL PROCEDURES

#### 3.1 Reagents and materials

Nickel Chloride Hexahydrate ( $\text{NiCl}_2 \cdot 6\text{H}_2\text{O}$ ) and Fluorine doped tin oxide coated glass (FTO Glass, with about 80% transmittance, 2.3 mm thickness and surface resistance of  $\sim 7 \Omega \cdot \text{sq}^{-1}$ ) were purchased from Sigma-Aldrich (USA), Potassium Chloride (KCl) was purchased from Dinâmica (Indaiatuba, Brazil), Potassium Nitrate ( $\text{KNO}_3$ ), Ruthenium(III) Chloride ( $\text{RuCl}_3$ ), Sulfuric acid ( $\text{H}_2\text{SO}_4$ ), Potassium Hexacyanoferrate ( $\text{K}_3[\text{Fe}(\text{CN})_6]$ ), Potassium ferrocyanide trihydrate ( $\text{K}_4[\text{Fe}(\text{CN})_6] \cdot 3\text{H}_2\text{O}$ ) were obtained from Acros Organics, Screen-Printed Carbon Electrode (CPE, Aux.:C; Ref.:C) was purchased from Metrohm. All solutions were prepared with Milli-Q water.

#### 3.2 Substrate preparation

FTO Glass was cut into  $2 \times 1$  cm rectangles. Subsequently, it was cleaned using a detergent and water solution and placed in an ultrasonic bath for 10 min. Afterward, it was rinsed with water and subjected to another 10 min cycle in the ultrasonic bath. Finally, it was washed with isopropyl alcohol and given another 10 min treatment in the ultrasonic bath. Following the cleaning process, the geometric area of the substrate was determined to be  $1 \text{ cm}^2$  using an isolator, and the substrates were placed in an oven at  $60 \text{ }^\circ\text{C}$  for drying.

#### 3.3 Anodic catalyst films preparation process

The catalyst films were prepared using a conventional three-electrode cell composed of a platinum wire as the counter electrode (CE), Ag/AgCl saturated as the reference electrode (RE), and FTO Glass substrate as the working electrode (WE). The electrochemical methods were performed on a Metrohm Autolab Potentiostat/Galvanostat, connected to a computer with NOVA 2.1.5 software.

##### 3.3.1 Metallic nickel film deposition

Firstly, nickel film was electrodeposited onto the substrate. The electrodeposition was conducted using a chronoamperometry method applying a potential of  $E_{\text{RHE}} = -1.3\text{V}$  for 60 seconds (until the charge reached 0.5 C on the working electrode) onto the substrate immersed in an acidified nickel chloride solution with 40 mL volume 0.05 M  $\text{NiCl}_2 \cdot 6\text{H}_2\text{O}$  in 0.1 M KCl and 5  $\mu\text{L}$  1 M  $\text{H}_2\text{SO}_4$  solution.

### 3.3.2 Nickel Prussian blue analogues film synthesis (NiHCF)

With the metallic film deposited onto the FTO substrate, the film is oxidized by applying a potential of  $E_{\text{RHE}} = + 1.5 \text{ V}$  for 250 seconds in 10 mM  $\text{K}_3[\text{Fe}(\text{CN})_6]$  with 0.1  $\text{KNO}_3$  solutions, forming a yellow-amber film using ferricyanide precursor. The obtained film was dried at 60 °C in an oven for 1 h.

### 3.3.3 Nickel Prussian blue analogues with cyanide vacancies film synthesis (NiHCF-vac)

To create cyanide vacancies by electrochemical method, the nickel metallic film was oxidized by applying a higher potential  $E_{\text{RHE}} = + 2.4 \text{ V}$  for 250 seconds in 10 mM  $\text{K}_3[\text{Fe}(\text{CN})_6]$  with 0.1 M  $\text{KNO}_3$  solution. The obtained films were dried at 60 °C in an oven for 1 h.

### 3.3.4 Nickel-Iron mixed oxides film synthesis (NiFeO<sub>x</sub>)

After the electrodeposition synthesis of nickel Prussian blue analogs (NiHCF and NiHCF-vac) in FTO substrate, the prepared films were heated in a tube furnace at 500 °C, in the air at 15 °C.min<sup>-1</sup> heating rate for 1 h. From this procedure, a mixed oxide film (NiFeO<sub>x</sub>) was obtained using Prussian blue analog as a precursor.

### 3.3.5 RuO<sub>2</sub> preparation film synthesis

An electrodeposited RuO<sub>2</sub> film on FTO was prepared for comparative effects and catalytic evaluation with the Prussian blue analogs and their oxides. Initially, a ruthenium metallic film was deposited onto FTO substrate by applying  $E_{\text{Ag}/\text{AgCl}} = - 0.6 \text{ V}$  for 300 s in a solution containing 10 mM  $\text{RuCl}_3$  in 0.1 M  $\text{KCl}$ . Then, ruthenium oxide film was prepared through a calcination process in a tube furnace at 450 °C, in air for 3 hours, at a 10 °C min<sup>-1</sup> heating rate<sup>20,21</sup>

## **3.4 Spectroscopy characterization techniques**

### 3.4.1 Electronic UV-Visible absorbance spectroscopy

Spectra of Nickel Prussian blue analogue films in the UV-Vis region were obtained using an Ocean Insight Flame Miniature UV-Visible absorption Spectrophotometer (Flam-S-UV-Vis series), with a quartz cuvette (1 cm optical path), from 200 to 900 nm.

### 3.4.2 Vibrational Raman spectroscopy

Raman spectra of the material were recorded on a Confocal Horiba Xplora spectrometer at an excitation wavelength of 785 nm with a (10x, 50x) objective

at room temperature in the range of 100 – 3000  $\text{cm}^{-1}$  and 10 % filter with 5 accumulations, and in 60 seconds, 1.74  $\mu\text{m}$  spot size and 4  $\text{cm}^{-1}$  resolution. The distance between the laser and the sample was adjusted using the camera coupled to the equipment to focus on the sample surface. The spectra were recorded after instrument calibration on the internal standard silicon wafer ( $\sim 520.7 \text{ cm}^{-1}$ ).

### **3.5 Microscopy characterization techniques**

#### 3.5.1 Scanning electron microscopy

The morphological images were obtained on a Quanta 250 field emission scanning electron microscope (FEI Co., USA) equipped with an Oxford X-MAX50 (Oxford, UK) X-ray dispersive spectrometer (EDS) were prepared on a conductive carbon tape followed by carbon powder coating on a Bal-Tec MD020 instrument (Balzers). The samples were previously coated with Iridium through sputtering.

#### 3.5.2 Atomic force microscopy

The topographic images were obtained on a FlexAFM C3000 – (Nanosurf, Switzerland) atomic force microscope operating a non-contact/tapping mode and recorded a 3  $\mu\text{m}$  image size in 1 second per point and 256 pixels points, 55 % Setpoint, 2000, 2400, and 0 as P-Gain, I-Gain and D-Gain values, respectively and 700 mV value for Free Vibration Amplitude acquisition properties.

### **3.6 Electrochemical characterization**

All electrochemical measurements were conducted in a  $\text{KNO}_3$  solution electrolyte, employing a typical three-electrode cell system using a platinum wire, saturated Ag/AgCl, and Catalysts films deposited onto FTO Glass as the counter electrode (CE), reference electrode (RE), and working electrode (WE), respectively.

#### 3.6.1 Cyclic voltammetry

The Cyclic Voltammetry was measured in the potential region by applying  $E_{\text{RHE}} = 0.2 \text{ V}$  to  $E_{\text{RHE}} = 1.2 \text{ V}$  at  $10 \text{ mV}\cdot\text{s}^{-1}$  scan rate for 2 scans.

#### 3.6.2 Linear sweep voltammetry

The voltammograms of the materials were measured in the potential region by applying  $E_{\text{RHE}} = 0.2 \text{ V}$  to  $E_{\text{RHE}} = 2.2 \text{ V}$  at  $5 \text{ mV}\cdot\text{s}^{-1}$  scan rate. The potential was corrected using 95 % of  $iR$  drop value for respectively material.

### 3.6.3 Electrochemical impedance spectroscopy

Impedance measurements for all the films were obtained by applying a  $E_{\text{RHE}} = 1.9 \text{ V}$  applying a frequency variation of  $1.10^6 \text{ Hz}$  to  $1.10^{-2} \text{ Hz}$ , 10 points per decade of a number of frequencies, and  $0.01 \text{ V}_{\text{RMS}}$  amplitude. The fit and simulation of the equivalent circuit used a typical Randles-Circuit.

### 3.6.4 Electrocatalytic evaluation tests

The potential conversion of the reference electrode ( $E_{\text{Ag/AgCl}}$ ) used to the reversible hydrogen electrode (RHE) was carried out using the following equation (4) and considering the pH of the  $\text{KNO}_3$  solution as 7.29 for all the electrochemical characterization used.

$$E \text{ vs. RHE} = E_{\text{Ag/AgCl}} + 0.059 \times \text{pH} + 0.197 \quad (4)$$

The oxidation overpotential ( $\eta_{\text{OER}}$ ) for current density was determined by correcting the thermodynamic potential of the water oxidation in pH 7 according to equation (5).

$$\eta_{\text{OER}} = V_{\text{onset,OER}} - 1.23 \quad (5)$$

Some aspects such as Tafel slope ( $\text{mv.dec}^{-1}$ ), overpotential ( $\eta$ ), onset (mV), and current density ( $j$ ) parameters were obtained by analyzing the Linear Sweep Voltammetry voltammograms for all the prepared catalysts.

## **3.7 Soft X-ray spectroscopy characterization**

The samples were analyzed at the IPE beamline of the Sirius facility at the Brazilian Synchrotron Light Laboratory using photoemission at A branch in the soft X-ray range (100 – 2000 eV). The samples were freshly prepared and kept in place using conductive carbon tape and silver ink, and then transferred to the vacuum chamber for 8 hours to minimize accumulation of contaminants at the surface.

### 3.7.1 X-ray Photoelectron spectroscopy

XPS spectra were performed using a PHOIBOS 150 analyzer from SPECS using a photon energy of 1200 eV using a pass energy of 20 eV. Due to observed surface charging in the samples during analysis, a flood gun beam was used to minimize this effect. Before collecting a complete set of spectra for each element, several survey scans were measured at different spots on the sample to evaluate sample homogeneity and eventual beam damage. Quantitative XPS analysis was performed by using the area

of the most intense peaks of each element after Shirley background removal correction by photoionization cross-section, inelastic mean free path, and ring current.

### 3.7.2 X-ray Absorption spectroscopy

Total electron yield (TEY) and Fluorescence yield (FY) XAS were obtained by measuring the drain current using a Stanford electrometer. A linear background was subtracted from the data and the intensities were normalized to 1 after the edges jump in Ni L-edges and Fe L-edges, respectively.

### **3.8 Supplementary measures**

Electronic absorbance spectra were obtained by UV-Visible spectroscopy of the following precursors:  $\text{NiCl}\cdot 6\text{H}_2\text{O}$ ,  $\text{K}_3[\text{Fe}(\text{CN})_6]$ ,  $\text{K}_4[\text{Fe}(\text{CN})_6]\cdot 3\text{H}_2\text{O}$  and NiHCF powders using ferricyanide and ferrocyanide. Vibrational spectra of NiHCF were obtained using ferricyanide and ferrocyanide precursors. To elucidate electronic and vibrational bands arising from the aforementioned precursors.

## 4. RESULTS AND DISCUSSION

### 4.1 Anodic catalyst film synthesis

#### 4.1.1 NiHCF

As described in section 3.3, the nickel Prussian blue analogue (NiHCF) was synthesized using an electrodeposition method divided into two stages using chronoamperometry, and all the results are shown in Figure 10. Firstly, a reduction potential is applied to the working electrode (FTO) immersed in a solution containing  $\text{Ni}^{2+}$  ions, in which the ions were reduced to metallic nickel (Figure 10A) due to the applied potential and deposited on the substrate as a film (equation 6).



After this first step, the metallic film was immersed in a solution containing ferricyanide  $[\text{Fe}(\text{CN})_6]^{3-}$  and an oxidation potential was applied, and the metallic nickel film was oxidized to  $\text{Ni}^{2+}$  ions which interacted with ferricyanide in the solution (equation 7), thus producing the NiHCF film electrochemically (Figure 10B)<sup>22,23</sup>.

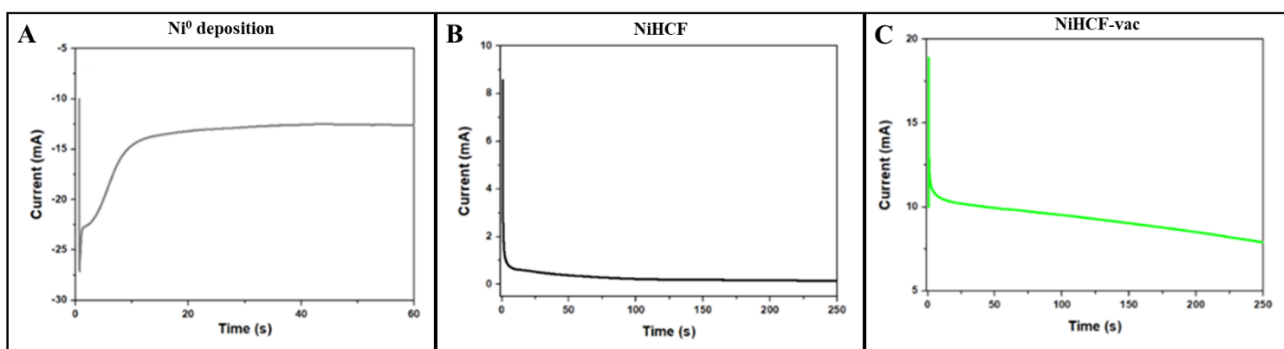


**Figure 10:** Chronoamperograms obtained for  $\text{Ni}^0$  (A), NiHCF (B) and NiHCF-vac (C) electrodeposition synthesis as pale-grey, black and green line, respectively.

To create cyanide vacancies ( $\text{v}_{\text{CN}}$ ) in NiHCF, it is necessary to apply a higher oxidation potential (Figure 10C) during the synthesis to oxidize some of the cyanide bridges during the nanomaterial synthesis process<sup>7,17,24</sup>. We believe that as cyanide bridges are removed from the structure, an aquo ligand ( $\text{H}_2\text{O}$ ) can be connected to the metal centers, which can increase their catalytic performance<sup>25</sup> proposed by the mechanism pathway that occurs in the WOR seen in Figure 11<sup>26</sup>. However, we must evaluate the creation of defects in the Prussian blue structure from spectroscopy, microscopy, and electrochemical studies.

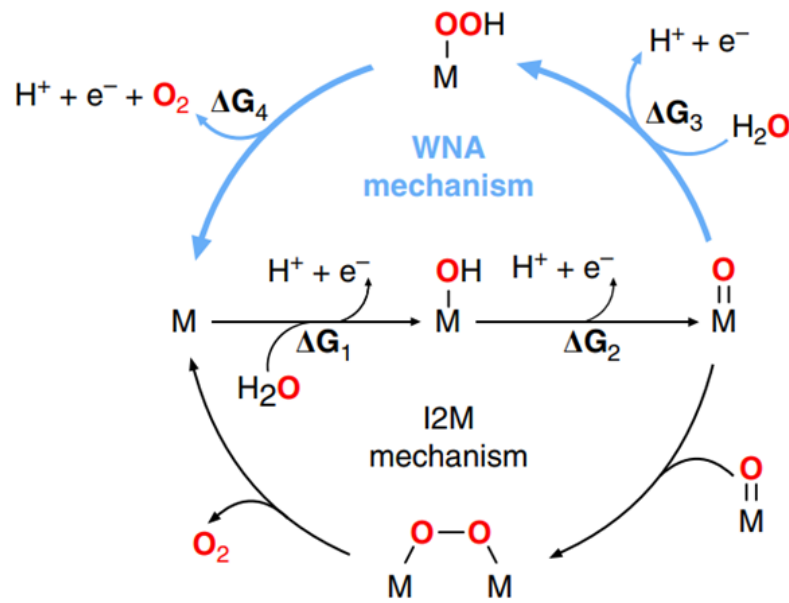


**Figure 11:** Catalytic cycle mechanism pathways proposed by the OER. (Craig, M. *et al.*)

#### 4.1.2 NiFeO<sub>x</sub>

One strategy studied by our research group<sup>6,27</sup> is the use of Prussian blue (PB) and its analogues (PBA) as a *template* precursor for the synthesis of its metal oxides through heat treatment (equation 8).



In this way, the films of the analogues produced without and with the insertion of cyanide vacancies in their structure were heat-treated using a tube furnace at a temperature of 500°C for 1 h. This process breaks the cubic structure of the PBA, allowing the metals to react with oxygen and form their oxides<sup>27,28</sup>.



As there are two different metals in their precursor structure, in this case, iron and nickel, it is possible that after heat treatment the material will produce a mixture of nickel oxides and iron oxides such as NiO, Fe<sub>2</sub>O<sub>3</sub>, and NiFe<sub>2</sub>O<sub>4</sub>, for example (equation 9)<sup>28</sup> and the complex mixture of its oxides mentioned after the thermal decomposition of NiHCF implies the improvement of the catalytic performance for anodic catalysts for water electrolysis.

### 4.1.3 RuO<sub>2</sub>

For a catalytic comparison study, ruthenium oxide (RuO<sub>2</sub>) deposited onto FTO was synthesized, applying a reduction potential in a solution containing ruthenium ions and subsequent heat treatment at 500°C for 3 h<sup>20,21</sup> as it is one of the state-of-art catalysts for WOR.

## **4.2 Electronic UV-Visible absorbance spectroscopy**

A study of the electronic configuration of the materials was carried out using the UV-Visible electronic absorbance spectroscopy, to investigate possible electronic changes in the ligand field transition metal-ligand charge transfer (MLCT) bands (~200 – 450 nm) regarding charge transfer intervalence band and d-d band (~550 – 800 nm) of iron and nickel<sup>29–32</sup>. The absorbance spectra of the nickel Prussian blue analogues films are shown in Figure 12.

It can be observed that both films present a similar profile but with some significant differences. Analyzing the region of the 200 nm – 450 nm in NiHCF (Figure 13A) and NiHCF-vac (Figure 13B) spectra, both materials have two bands which are associated with the  ${}^1T_{1g} \leftarrow {}^1A_{1g}$  and  ${}^3T_{1g} \leftarrow {}^1A_{1g}$ , it is possible to verify the bathochromic effect in the NiHCF-vac spectrum for these bands, as they moved to higher wavelengths from 321 nm to 330 nm and from 388 nm to 412 nm (Table 2), indicating that there was some electronic modification regarding the ligand-metal-ligand band after the defect creation process.<sup>33,34</sup>

Analyzing the intervalence charge transfer and d-d bands region (550 nm – 800 nm), it can be seen a d-d band in ~550 nm attributed with d-d Ni (d<sup>8</sup>) in a highly displaced octahedral complex in the hexacyanometallate structure. However, the assigned charge transfer intervalence band (600 nm – 800 nm) attributed for Fe (d<sup>5</sup>) to Fe (d<sup>6</sup>) in which the NiHCF-vac spectra exhibit this band shifted to a shorter wavelength from 726 nm to 691 nm (Table 2)<sup>34,35</sup>.

This indicates that the creation of defects in the structure had significant effects on the electronic characteristics of the cyanometallate complex. It is also important to highlight that this shift may have a certain contribution from its precursors such as ferricyanide and nickel (Table 2).

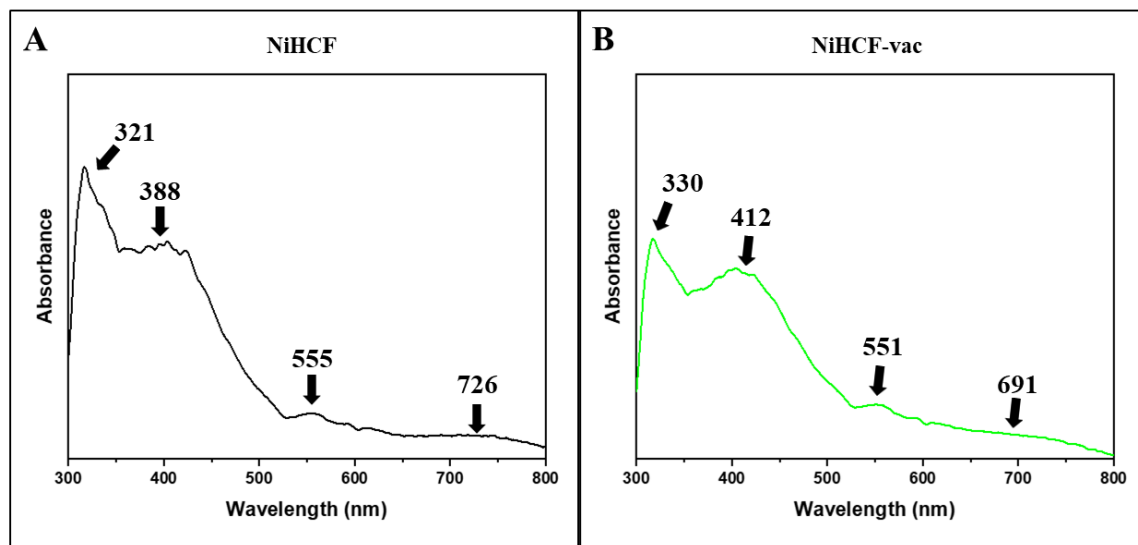


**Figure 12:** Electronic spectroscopy UV-visible absorbance study of NiHCF (A) and NiHCF-vac (B) films in black and green line, respectively.

**Table 2:** Electronic absorbance UV-Vis band and their respectively assignment for NiHCF and NiHCF-vac and the comparison with PB, BG and their respectively precursors.

Materials	Band <sub>1</sub> (nm)	Assignment	Band <sub>2</sub> (nm)	Assignment	Band <sub>3</sub> (nm)	Assignment	Band <sub>4</sub> (nm)	Assignment
NiHCF	321	${}^1T_{1g} \leftarrow {}^1A_{1g}$	388	${}^3T_{1g} \leftarrow {}^1A_{1g}$	555	d-d ( $Ni^{II}$ )	726	Intervalece Charge Transfer
NiHCF-vac	330	${}^1T_{1g} \leftarrow {}^1A_{1g}$	412	${}^3T_{1g} \leftarrow {}^1A_{1g}$	551	d-d ( $Ni^{II}$ )	691	Intervalece Charge Transfer
NiHCF( $Fe^{II}$ )	310	${}^1T_{1g} \leftarrow {}^1A_{1g}$	-	-	-	-	-	-
NiHCF( $Fe^{III}$ )	313	${}^1T_{1g} \leftarrow {}^1A_{1g}$	413	${}^3T_{1g} \leftarrow {}^1A_{1g}$	-	-	-	-
$NiCl_2 \cdot 6H_2O$	395	${}^3T_{1g} (P) \leftarrow {}^3A_{2g}$	661	${}^1E_g \leftarrow {}^3A_{2g}$	723	${}^3T_{1g} (F) \leftarrow {}^3A_{2g}$	-	-
$K_3[Fe(CN)_6]$	305	${}^1T_{1g} \leftarrow {}^1A_{1g}$	423	${}^3T_{1g} \leftarrow {}^1A_{1g}$	-	-	-	-
$K_4[Fe(CN)_6] \cdot 3H_2O$	316	${}^1T_{1g} \leftarrow {}^1A_{1g}$	-	-	-	-	-	-
PB	408	${}^3T_{1g} \leftarrow {}^1A_{1g}$	710	Intervalece Charge Transfer	-	-	-	-
BG	304	${}^1T_{1g} \leftarrow {}^1A_{1g}$	421	${}^3T_{1g} \leftarrow {}^1A_{1g}$	757	Intervalece Charge Transfer	-	-

For comparison with spectrum catalysts films to analogue powders ( $NiHCF(Fe^{II})$  and  $NiHCF(Fe^{III})$ ), UV-vis spectra of the analogues using ferrocyanide and ferricyanide precursors both dispersed in water, were also obtained (Table 2), where some bands coincide with those reported in Figure 12. However, it is not possible to see the bands between 550 nm – 800 nm region. Since the NiHCF films were obtained from a ferricyanide precursor solution, the spectra of the films are more similar to the  $NiHCF(Fe^{III})$  spectra. It is important to highlight that the first band of both films is not symmetrically to that of the analogue dispersed in solution, indicating the presence of  $Fe^{2+}$  in the structure of the material obtained in the films.

### 4.3 Vibrational Raman spectroscopy

Raman spectroscopy allows for the analysis of molecular vibrational modes and provides us with fingerprint bands that can be identified. The vibrational spectroscopy

spectra of the nickel Prussian blue analogues are presented in Figure 13. As predicted, both materials exhibit bands between 2000 - 2200  $\text{cm}^{-1}$  in the spectra, which are attributed to the stretching of  $\nu(\text{CN})$  in the structure<sup>16</sup>. These are fingerprint bands for cyanometallates materials, corresponding to the  $A_{1g}$  and  $E_g$  vibrational modes (Table 3)<sup>7,18,29</sup>. It can be noted that  $\nu(\text{CN})$  band region in NiHCF-vac is shifted to higher wavenumbers from 2088  $\text{cm}^{-1}$  and 2118  $\text{cm}^{-1}$  to 2147  $\text{cm}^{-1}$  and 2180  $\text{cm}^{-1}$ . In addition to  $\nu(\text{CN})$ , the cyano complexes exhibit  $\nu(\text{MC})$ ,  $\delta(\text{MCN})$  and  $\delta(\text{CMC})$  band in the low-frequency region (100  $\text{cm}^{-1}$  – 600  $\text{cm}^{-1}$ ) for both materials but the vibrational modes of NiHCF-vac are shifted to shorter wavenumbers compared to NiHCF (Table 3)<sup>17,18</sup>.

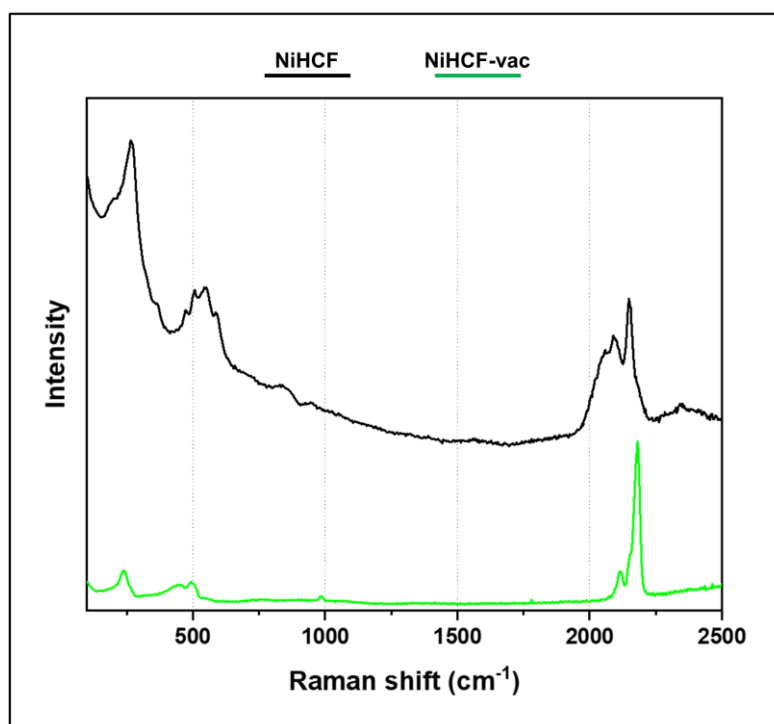


**Figure 13:** Vibrational Raman spectroscopy for NiHCF and NiHCF-vac in black and green solid lines respectively.

**Table 3:** Raman vibrational modes assignment for NiHCF and NiHCF-vac materials.

Materials	Raman shift ( $\text{cm}^{-1}$ )				
	Vibrational mode assignment				
	$\delta(\text{CFeC})$	$\delta(\text{FeCN})$	$\nu(\text{FeC})$	$\nu(\text{CN})$	
$A_{1g}$				$E_g$	
NiHCF	264	471	506	2088	2147
NiHCF-vac	241	444	489	2118	2180

This shift can be understood from the higher bond force constant ( $\kappa$ ) of the analogue with defects compared to the conventional analogue, which is directly

proportional to the wavelength ( $\nu$ ) (equation 10), and it helps to minimize the losses of some cyanides in its structure. This can be related to the fact that higher metal oxidation states can strengthen  $\sigma$ -bonding and since electrons are removed from a weakly anti-bonding orbital, the metallic centre oxidation can result in the increase of the  $\nu_{(\text{CN})}$ , thus, shifting the bands towards higher wavelengths<sup>7,25</sup>.

$$\nu = \frac{1}{2 \times \pi} \times \sqrt{\frac{\kappa}{\mu}} \quad (10)$$

Furthermore, the Raman spectrum of NiHCF was compared with NiFeO<sub>x</sub> (Figure 14), in which the disappearance of the cyanide  $\nu(\text{CN})$  stretch of NiFeO<sub>x</sub> was seen after heat treatment, indicating the decomposition of the cyanometallate structure thermally, forming mixed oxides composed of iron and nickel. We can verify some signature stretches of Fe<sub>2</sub>O<sub>3</sub>, NiO and NiFe<sub>2</sub>O<sub>4</sub> with the vibrational modes being in 248 cm<sup>-1</sup> ( $\delta E_g(\text{Fe-O})$ ), 403 cm<sup>-1</sup> (TO) and 700 cm<sup>-1</sup> ( $\nu A_{1g}(\text{Fe-O})/(\text{Ni-O})$ ),<sup>36-38</sup> respectively. demonstrating that NiFeO<sub>x</sub> is composed of a complex mixture of iron and nickel oxides.

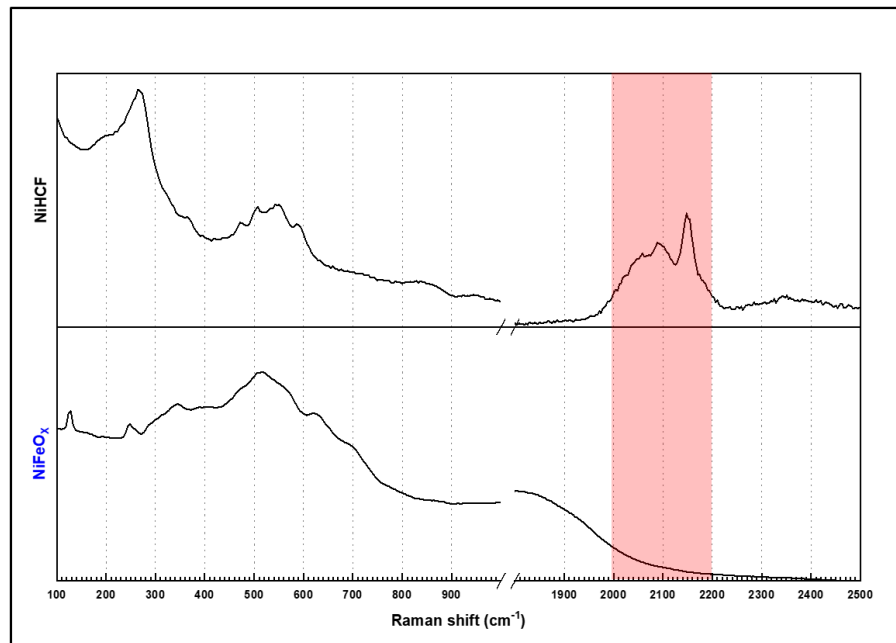


**Figure 14:** Vibrational Raman spectroscopy comparison to NiHCF to NiFeO<sub>x</sub> spectra.

## 4.4 Microscopy characterization

### 4.4.1 Scanning electronic microscopy

Using scanning electron microscopy (SEM), we aimed to obtain information on how the analogue films were dispersed and deposited on the substrate and to understand

if the introduction of vacancies had any morphological effect on the samples. Additionally, we performed elemental mapping of the components in the nickel Prussian blue structure.

Analyzing at high magnification to verify the cubic structure of the material, we can see morphological differences between the nickel analogue with and without defects (Figure 15). The NiHCF presents a relatively well-defined cubic morphology, while the NiHCF-vac is significantly more amorphous and more aggregated cubes its structure is less defined<sup>32,39-41</sup>. Thus, the implementation of defects also impacts the morphological aspects of the material.

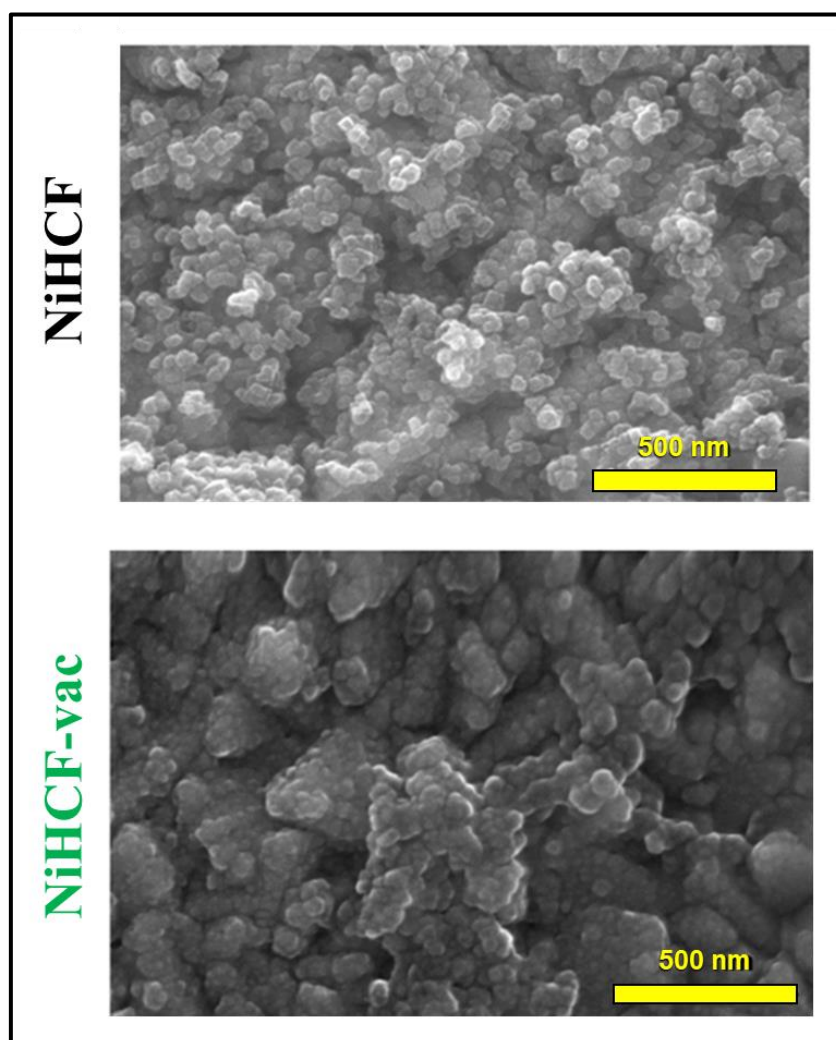


**Figure 15:** Morphological studies structures in NiHCF and NiHCF-vac, using scanning electron microscopy.

Furthermore, the NiHCF is more evenly covered and dispersed on the substrate while the NiHCF-vac presents darker regions associated with the underlying substrate (Figure 16). This can be related to the synthesis process, as creating the material with

defects requires applying a higher oxidation potential ( $E_{\text{RHE}} = 2.4 \text{ V}$ ), which is above the oxidation potential of water ( $E = 1.23 \text{ V}$ ). This process produces oxygen bubbles on the surface, exposing some parts of the substrate when preparing the material with defects.

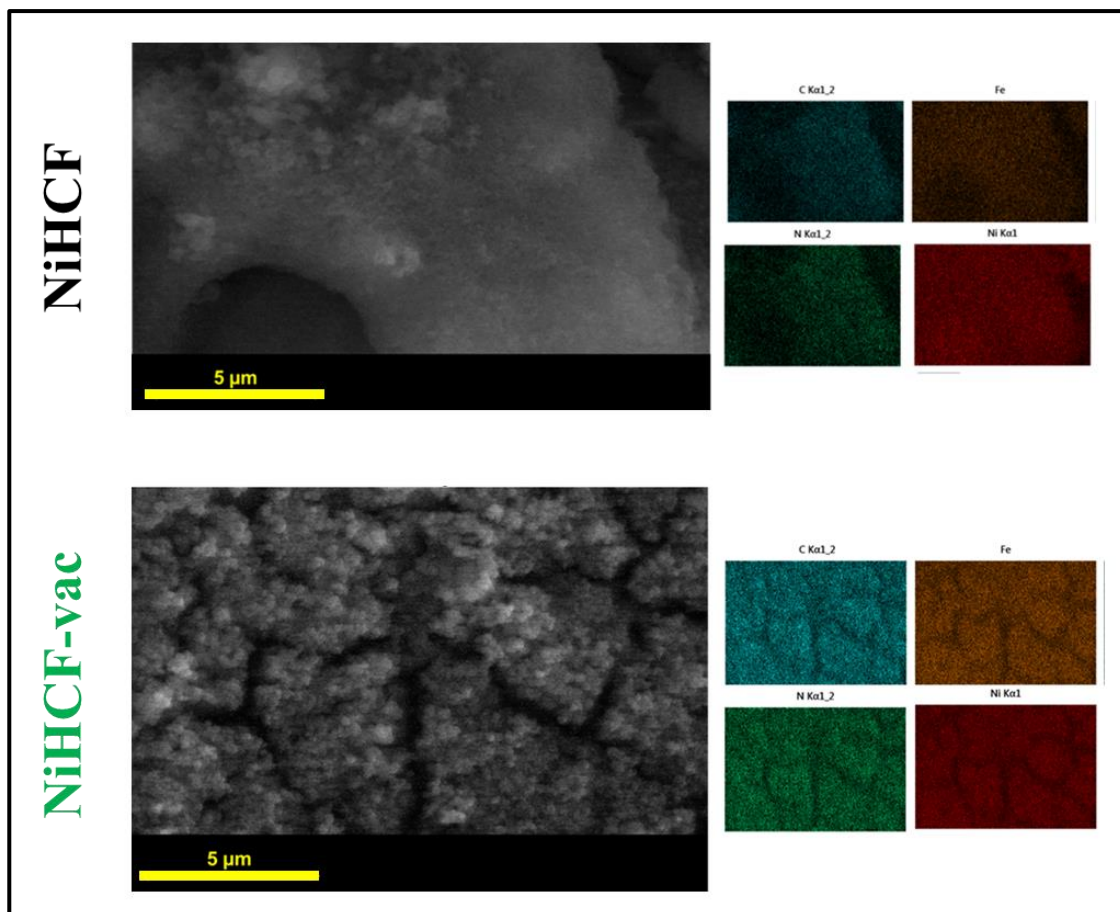


**Figure 16:** Scanning electron microscopy (SEM) and mapping elements of C, Fe, N and Ni by EDS for NiHCF and NiHCF-vac in 5 μm.

#### 4.4.2 Atomic force microscopy

Atomic force microscopy provides information on how the material is dispersed on the FTO glass substrate gathered by the “feeling” or “touching” the surface with a mechanical probe which gives additional information on the topography, thickness, and roughness ( $S_q$ ) aspects of the sample<sup>22</sup>. The topography and average

roughness values of the FTO glass substrate, NiHCF, NiHCF-vac, and the thermally treated analogues ( $\text{NiFeO}_x$ ) were analyzed.

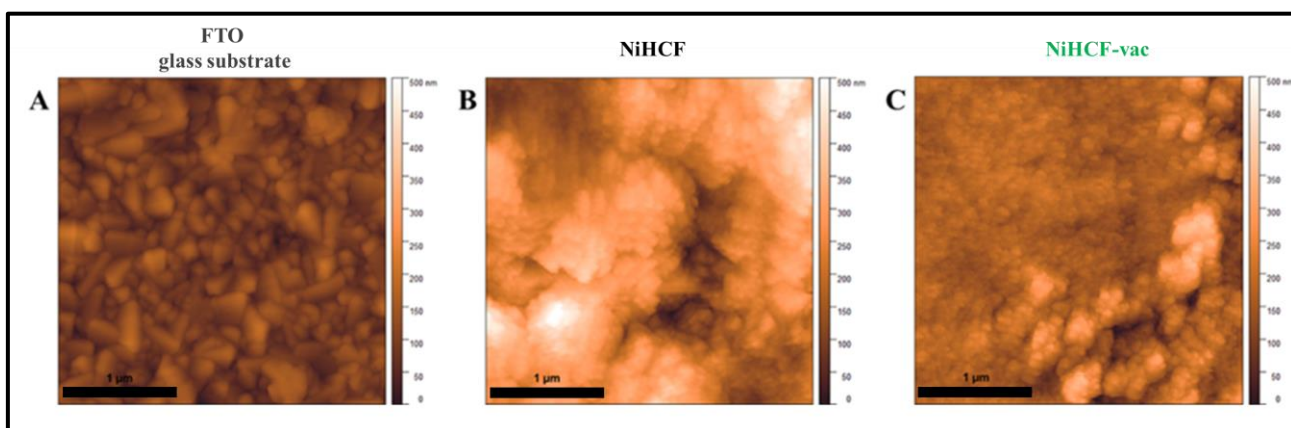


**Figure 17:** Atomic force microscopy topography image. FTO glass substrate (A), NiHCF (B) and NiHCF-vac, respectively.

It can be observed that both NiHCF and NiHCF-vac films (Figure 17) covered the substrate (Figure 17A) relatively well. However, the NiHCF-vac (Figure 17C) in its structure presents a relatively lower topographic film height compared with the NiHCF (Figure 17B), with values of  $0.38 \mu\text{m}$  and  $0.52 \mu\text{m}$  respectively (Figure 18). As mentioned in section 3.3.3, this decrease in thickness is associated due to the application of a high oxidation potential during its electrochemical synthesis by lixiviation during water oxidation reaction, which leads to a reduction in the film roughness factor ( $S_q$ ) from  $58.02 \text{ nm}$  to  $38.52 \text{ nm}$  for the materials without and with defects in the structure, respectively.

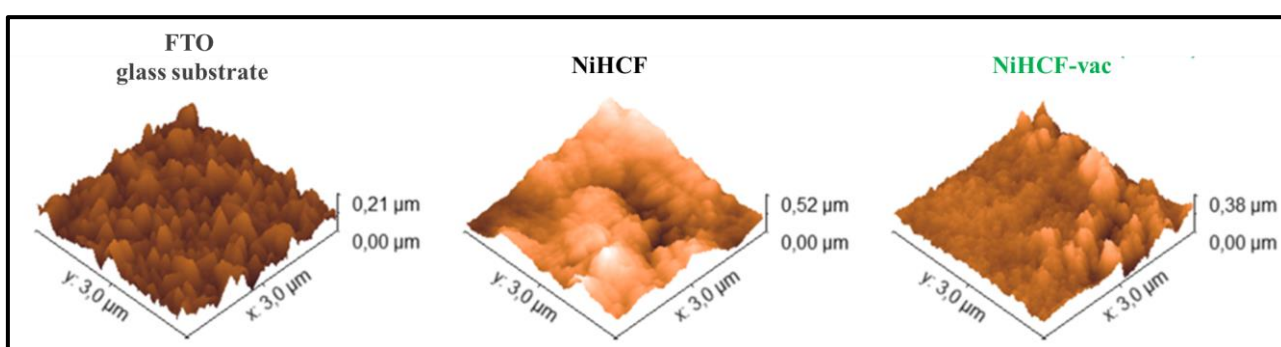


**Figure 18:** Atomic force microscopy 3D topography image. Left to right. FTO glass substrate, NiHCF and NiHCF, respectively.

For the analogues that passed by thermal treatment ( $\text{NiFeO}_x$  and  $\text{NiFeO}_{x-\text{vac}}$ ) its topographical appearance has changed, indicating a change from cyanometallate to its mixed oxides mentioned. However, analyzing only the materials after heat treatment, there is no significant topological difference compared to each other (Figure 19). The thickness has changed from  $0.52 \mu\text{m}$  to  $0.37 \mu\text{m}$  ( $\text{NiHCF} \rightarrow \text{NiFeO}_x$ ) and from  $0.38 \mu\text{m}$

to  $1.16 \mu\text{m}$  (NiHCF-vac  $\rightarrow$  NiFeO<sub>x</sub>-vac) (Figure 20) and the roughness value (Sq) from 90,16 nm to 52.13 nm. All the roughness values for all materials are shown in Table 5. To obtain more information, it is necessary to conduct scanning electron microscopy studies of these materials.

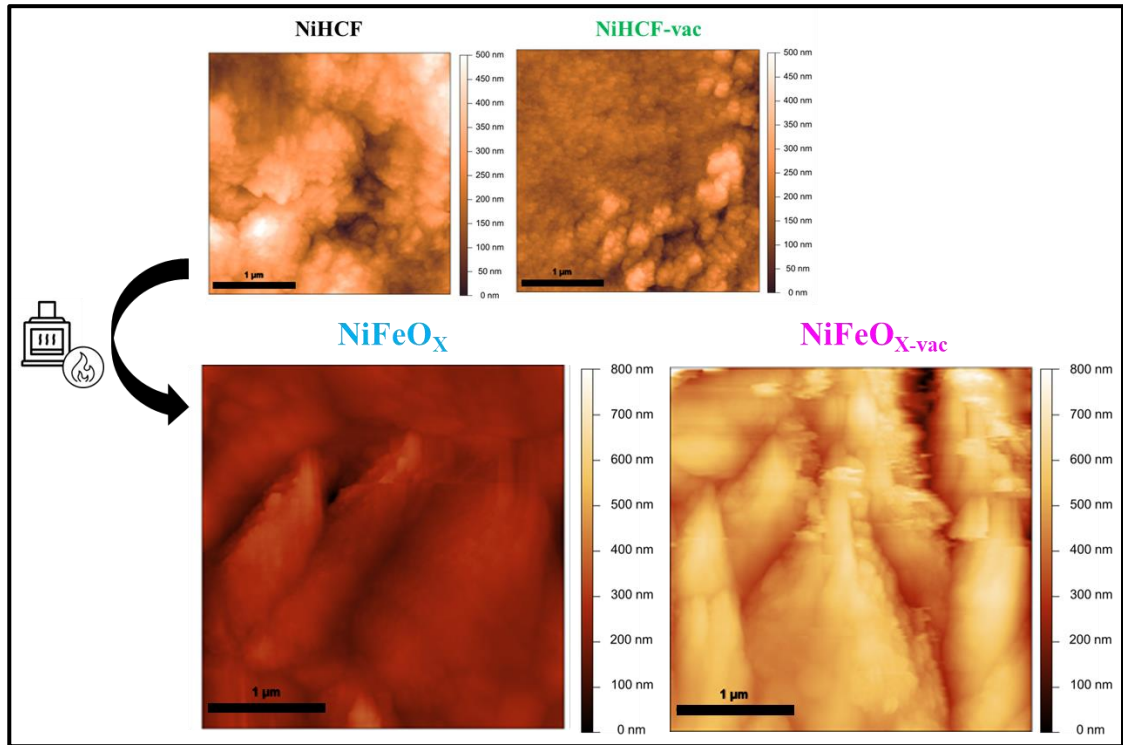


**Figure 19:** Atomic force microscopy topography image for NiHCF after heat treatment. NiFeO<sub>x</sub> and NiFeO<sub>x</sub>-vac

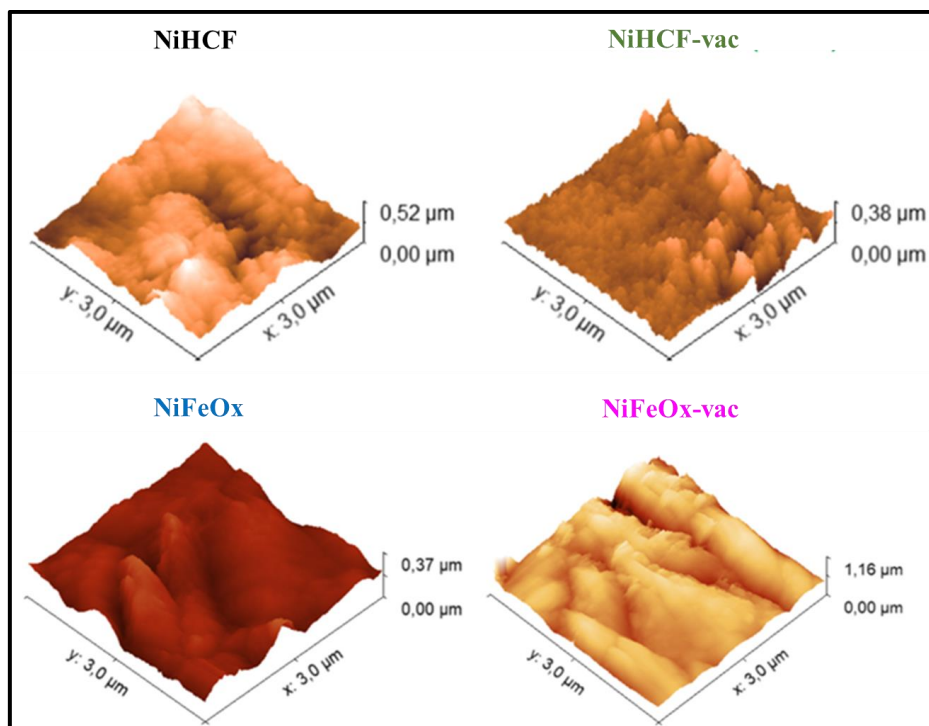
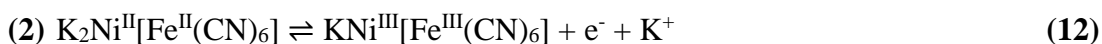
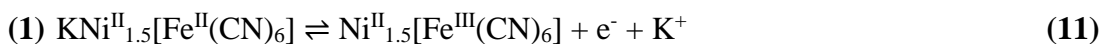


**Figure 20:** Atomic force microscopy 3D topograph images comparison from NiHCFs to NiFeOx.

## 4.5 Electrochemical studies

### 4.5.1 Cyclic voltammetry

Cyclic voltammetry was performed at a scan rate of  $50 \text{ mV}\cdot\text{s}^{-1}$  in a  $0.5 \text{ mol}\cdot\text{L}^{-1}$   $\text{KNO}_3$  electrolyte solution with pH 7.29 to provide results on redox processes occurring within the potential range between  $E_{\text{Ag}/\text{AgCl}} = 0.0 \text{ V}$  to  $E_{\text{Ag}/\text{AgCl}} = 1.0 \text{ V}$  of the NiHCFs materials. The results of the voltammograms are shown in Figure 22. It is possible to verify two redox processes (1 and 2) in nickel Prussian analogue films in the potential of  $E_{\text{RHE}} = 1.2 \text{ V}$  and  $1.4 \text{ V}$ , which are attributed to oxidation and reduction of iron and nickel species  $\text{Fe}^{\text{II}}/\text{Fe}^{\text{III}} - \text{CN} - \text{Ni}^{\text{II}}/\text{Ni}^{\text{III}}$  in the anodic catalysts differentiating the stoichiometric formation of the NiHCF material and the iron redox processes from two following reactions



The (1) process is associated the stoichiometric formation for  $\text{KN}_{1.5}[\text{Fe}(\text{CN})_6]$  and the (2) is for the stoichiometric formation for  $\text{K}_2\text{Ni}[\text{Fe}(\text{CN})_6]$  due to the formation of the material seen in equation 12, as it has more potassium in its structure, the intercalation of the cation in its structure is difficult, requiring a greater potential for the oxidation and reduction process of iron species to occur compared to that seen in equation 11<sup>22,30</sup>. From the voltammograms (Figure 21), the NiHCF-vac material has

these redox peaks at 1.24 V and 1.37 V for  $E_{\text{peak1}}$  and at 1.35 V and 1.20 V for  $E_{\text{peak2}}$  (green line), while the NiHCF material has peak potentials at  $E_{\text{peak1}}$  of 1.23 V and 1.35 V and at  $E_{\text{peak2}}$  of 1.29 V and 1.19 V (black line). We can conclude that the insertion of defects in the structure shifted the redox peak potentials to slightly higher values (Figure 22). Furthermore, the peak variation ( $\Delta E_{\text{peak}}$ ) of the material is associated of the reversibility of the process with vacancies is smaller than that of the material without defects, with peak values of 40 mV and 24 mV for the material with vacancies, and 51 mV and 30 mV for the one without vacancies, respectively.

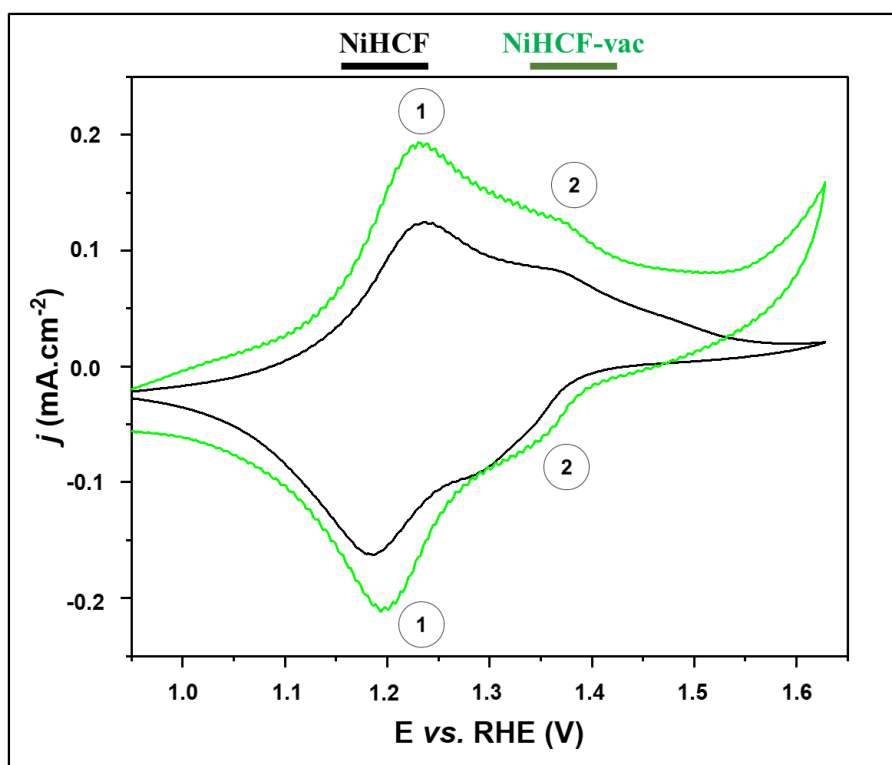


**Figure 21:** Cyclic voltammogram for NiHCFs in 0.5 M  $\text{KNO}_3$  pH 7.29 condition. NiHCF and NiHCF-vac in black and green lines, respectively.

#### 4.5.2 Electrochemical impedance spectroscopy

Electrochemical impedance spectroscopy (EIS) was conducted on the material and the substrate under the same electrolyte solution conditions, but applying a potential of  $E_{\text{Ag}/\text{AgCl}} = 1.7$  V ( $E$  vs RHE = 2.31 V) standardised potential value for the overpotential necessary for water oxidation to occur in the FTO glass substrate. The Nyquist plots, characterized by a semi-circular behaviour, provide information about the physical resistance, such as resistance solution ( $R_s$ ), charge transfer resistance ( $R_{\text{ct}}$ ) and the double-layer capacitance ( $Q_{\text{DL}}$ ) during the electrochemical process<sup>42</sup>.

Analyzing the Nyquist plots results, we can see that both the substrate and the nickel Prussian blue analogues and their oxide exhibit semicircular behaviour. Thus, with an adapted Randles's equivalent circuit (Figure 22), where  $R_s$  is the solution resistance to the electrode,  $R_{ct}$  is the charge transfer resistance, and  $Q_{DL}$  is a constant phase element that can act as a hybrid of a capacitor or resistor (in which when its  $N$  value is greater than 0.5 it can be more capacitive than resistive characteristics), it is possible to give us the value of  $R_{ct}$  for the materials one of the factors that the lower the  $R_{ct}$  value is, the better the charge transfer the material is. The Nyquist plots are shown in Figure 23.

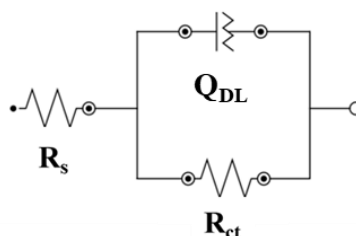


**Figure 22:** Adapted Randle's circuit for fitting simulation for EIS results.

The height of the semicircles is quite significant between the FTO glass substrate, and the material deposited on it, with the NiHCF-vac the smallest semicircle height, which is directly related to the charge transfer through the electrode during an electrochemical process. Comparing the NiHCFs each other (Figure 23A) the charge transfer resistance values for the analogue with vacancies (green line) are  $63.6 \Omega$ , and  $234 \Omega$  for the conventional material (black line). Comparing the NiHCF to NiFeOx (Figure 23B), the second one exhibits a lower  $R_{ct}$  than NiHCF, from  $232 \Omega$  to  $18.9 \Omega$ , respectively (Table 4). The lower charge transfer resistance value indicates that the defects engineering and the thermal decomposition facilitated the charge transfer process of the material as an electrode.

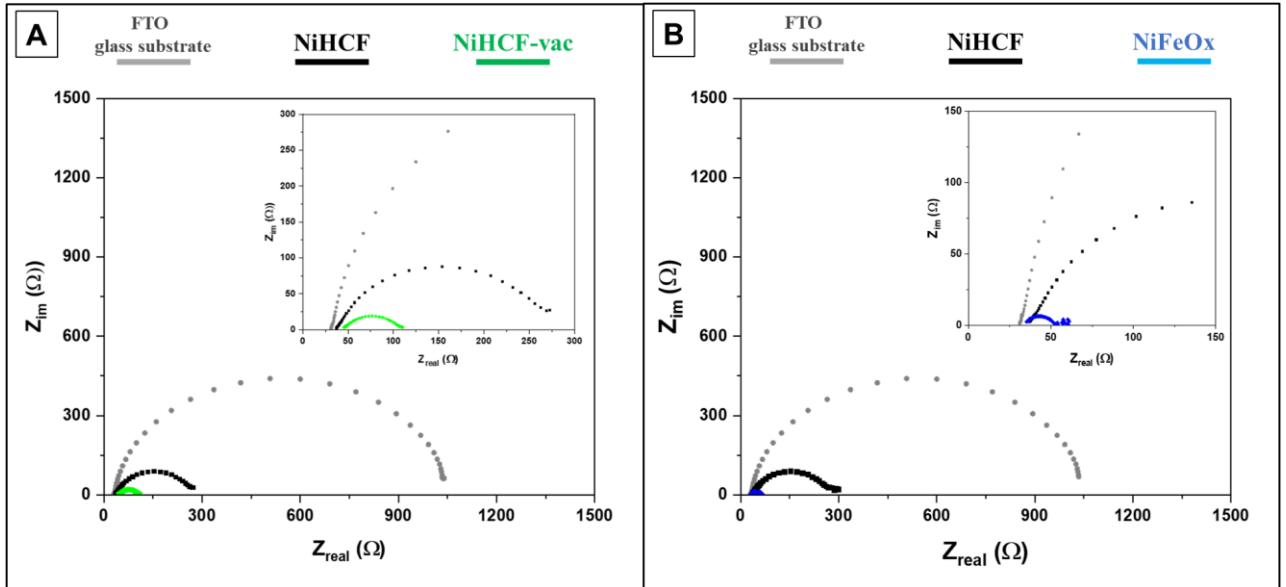


**Figure 23:** Electrochemical impedance spectroscopy Nyquist plot for FTO glass substrate, NiHCF and NiHCF-vac in pale-grey, black and green line (A) and comparison from NiHCF to NiFeO<sub>x</sub> in blue line (B), respectively at 2.31 V E vs. RHE (1.7 V in E<sub>Ag/AgCl</sub>), from 5.10<sup>5</sup>Hz to 0,005 Hz.

**Table 4:** Electrochemical results obtained using electrochemical impedance spectroscopy. To calculate ECSA value, we use Q<sub>DL</sub> divided by the C<sub>s</sub> as 35 μF.cm<sup>-2</sup>.

Materials	R <sub>ct</sub> (Ω)	Q <sub>DL</sub> (μF)	χ <sup>2</sup>	ECSA*
FTO	1002	10.28	0.116	0.293
NiHCF	234	63.53	0.042	1.787
NiHCF-vac	63.6	47.03	0.011	1.343
NiFeO <sub>x</sub>	18.9	46.83	0.001	1.338

Another aspect that we can calculate is the electrochemically surface active area (ECSA) of the materials considering Q<sub>DL</sub> as a double-layer capacitance divided with the specific capacitance (C<sub>s</sub>) of conventional PBAs as 35 μF.cm<sup>-2</sup> (Equation 13). Although NiHCF-vac and NiFeO<sub>x</sub> have better charge transfer, their ECSA is relatively lower (1.343 cm<sup>-2</sup> and 1.338 cm<sup>-2</sup>) compared to NiHCF (1.787 cm<sup>-2</sup>), this implies a higher current density (*j*) for these materials after the defects insertion and heat treatment processes.

$$\text{ECSA} = \frac{Q_{\text{DL}}}{C_s} \quad (13)$$

### 4.5.3 Linear sweep voltammetry

Through linear voltammetry, we can verify when the water oxidation reaction starts, determining the onset potential value (Figure 24). It is possible to analyze the onset value among the analogues (black and green lines) and the obtained oxides (blue and pink lines): the only difference between the samples before and after thermal treatment is the current density, which is higher for the calcinated samples and, between the oxides ( $\text{NiFeO}_x$  and  $\text{NiFeO}_{x-\text{vac}}$ ), is higher for the one with defects ( $\text{NiHCF-vac}$ ). Using a normalized current density considering a geometric area of  $1 \text{ cm}^2$ , we can deduce from the voltammogram of the NiHCFs that the onset ( $\eta$ ) of the material with cyanide vacancies ( $\text{NiHCF-vac}$ ) is lower compared to the conventional material (Figure 24A), changing from 821 mV to 774 mV, respectively. Thus, we can conclude that the creation of defects in catalysts by electrochemical methods positively influenced the catalysis of the water oxidation reaction<sup>15,17,41,42</sup>.

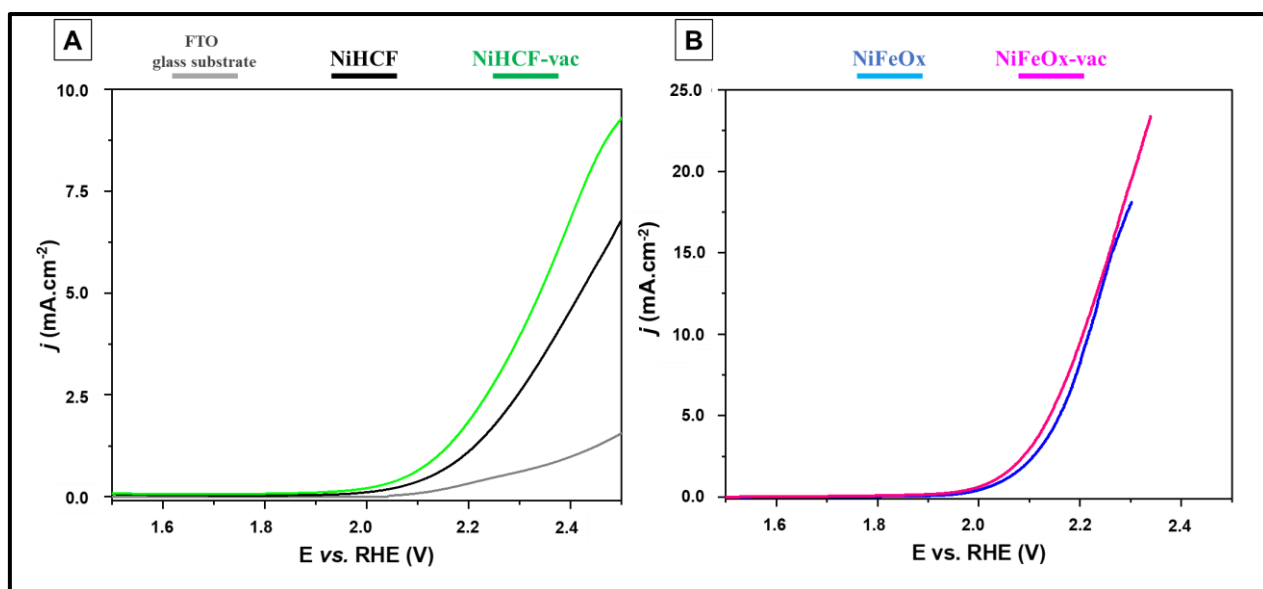


**Figure 24:** Left to right. Linear sweep voltammetry for FTO glass substrate, NiHCF, NiHCF-vac,  $\text{NiFeO}_x$  and  $\text{NiFeO}_{x-\text{vac}}$  in pale-grey, black, green, blue and pink line, respectively at scan rate  $5 \text{ mVs}^{-1}$ .

Furthermore, the onset of the analogues after the thermal treatment has a lower onset value than their respective precursor, changing from 740 mV to 730 mV for  $\text{NiFeO}_x$  and  $\text{NiFeO}_{x-\text{vac}}$  respectively (represented as a blue and pink line in Figure 24B). On the other hand, when the analogues undergo the thermal treatment process<sup>6,28</sup>, implying that despite structural differences in the precursor are not significant differences in their onset for the water oxidation reaction catalysis.

#### 4.6 Electrocatalysis evaluation parameters

From the linear sweep voltammogram, it is possible to extract electrocatalytic parameters such as the onset of the reaction and, most importantly, the Tafel slope. The Tafel slope, a kinetic parameter, relates the overpotential of the material to the logarithm of the current density passing through the electrode. The lower its value for certain materials, the higher is its catalytic performance<sup>9,10</sup>. The graph with the Tafel slopes of the materials is shown in Figure 25.

It is observed that between the NiHCF (black line) and NiHCF-vac (green line), the value decreased from 204 mV.dec<sup>-1</sup> to 201 mV.dec<sup>-1</sup>. The decrease in the Tafel slope, indicates a faster kinetic parameter. Furthermore, NiFeO<sub>x</sub> films (blue line) and NiFeO<sub>x-vac</sub> (pink line) show lower Tafel slope values compared to their precursor (NiHCF), with 154 mV.dec<sup>-1</sup> and 152 mV.dec<sup>-1</sup>, respectively.

All electrocatalytic parameters obtained from the materials can be seen in Table 5, comparing their results with conventional Prussian Blue and RuO<sub>2</sub> under mild conditions for the water oxidation reaction. For electrocatalytic comparison studies, all the materials have a better performance towards water oxidation reaction compared to PB. Comparing to RuO<sub>2</sub> catalyst (cyan line) was used since this is one of the state-of-the-art anode catalysts for the water oxidation reaction. Analogues that underwent thermal treatment achieved values close to RuO<sub>2</sub> a small difference between 20 mV to NiFeO<sub>x</sub>.

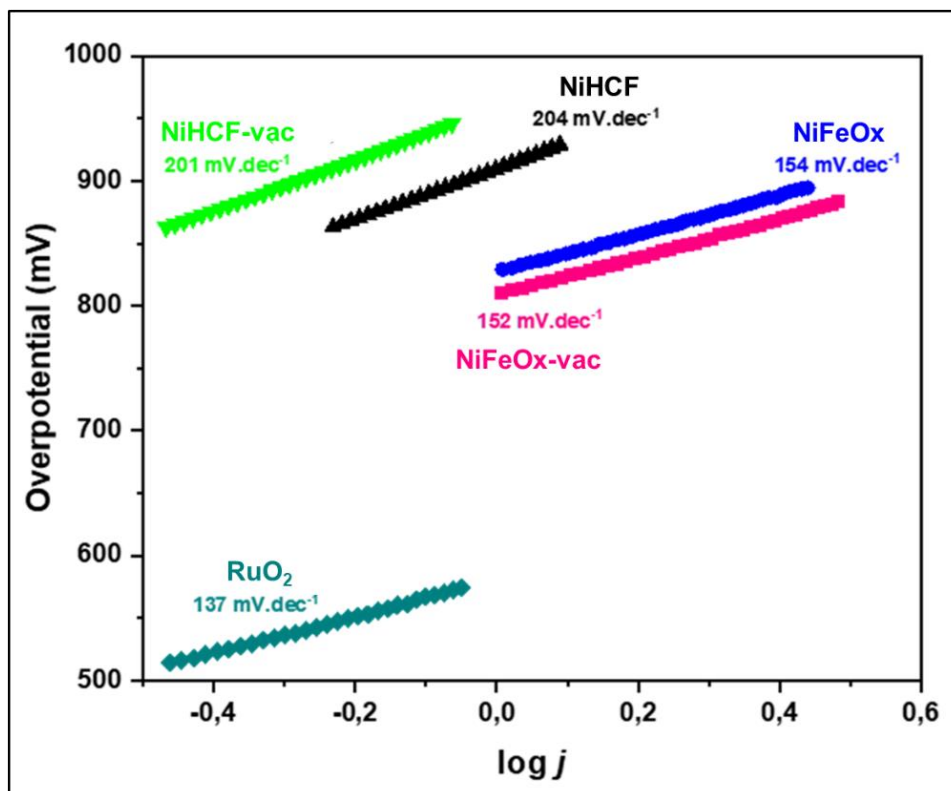


**Figure 25:** Tafel plot for NiHCF, NiHCF-vac, NiFeO<sub>x</sub>, NiFeO<sub>x</sub>-vac and RuO<sub>2</sub> in black, green, blue, pink and cyan line, respectively.

**Table 5:** Electrocatalysts parameters obtained and comparison with Prussian Blue (PB) and RuO<sub>2</sub> for anodic catalysts for water electrolysis under mild conditions. \*The PB use a different working electrode (GC) and method to calculate ECSA.

	Rct (Ω)	ECSA (cm <sup>2</sup> )	Sq (nm)	Overpotential (mV)	Tafel slope (mV.dec <sup>-1</sup> )	Ref.
<b>PB</b>	840	0,092*	-	971	247	[7]
<b>NiHCF</b>	234	1.787	52.0	821	204	This work
<b>NiHCF-vac</b>	63.6	1.343	38.0	774	201	This work
<b>NiFeOx</b>	18.9	1.338	37,0	740	154	This work
<b>NiFeOx-vac</b>	-	-	116,0	730	152	This work
<b>RuO2</b>	-	-	31.0	578	137	-

## 4.7 Soft X-ray spectroscopy characterization

### 4.7.1 X-ray photoelectron spectroscopy

Synchrotron-based soft X-ray photoelectron spectroscopy (XPS), performed at the IPÊ synchrotron light beamline at LNL-Sirius, was used to analyze the surface composition and chemical speciation of Ni and Fe elements in the films produced within the binding energy range of 900 eV to 0 eV. The survey graph is presented in Figure 26.

Analyzing the nickel Prussian blue analogues (black and green lines) (Figure 26A), we can see that both present the same chemical composition, identifying Ni 2p (853 eV), Fe 2p (708 eV), N 1s (398 eV), and C 1s (283 eV), with Sn 3d (485 eV) and O 1s (531 eV) coming from the substrate (grey line)<sup>16,18,39</sup>. It is possible to observe a decrease in the N 1s and C 1s peaks (maximum value of the peak at the theoretic binding energy) of the analogue with defects (green line), considering the atomic percentage of N 1s and C 1s (Table 6) from 15.29 and 18.87 to 9.83 and 9.85 NiHCF and NiHCF-vac respectively, moreover has a lower maximum peak intensity losses of 33% and 37% intensity for N 1s and C 1s<sup>17,18</sup>. This strongly indicates that the analogue with vacancies has fewer cyanide bonds in its structure.

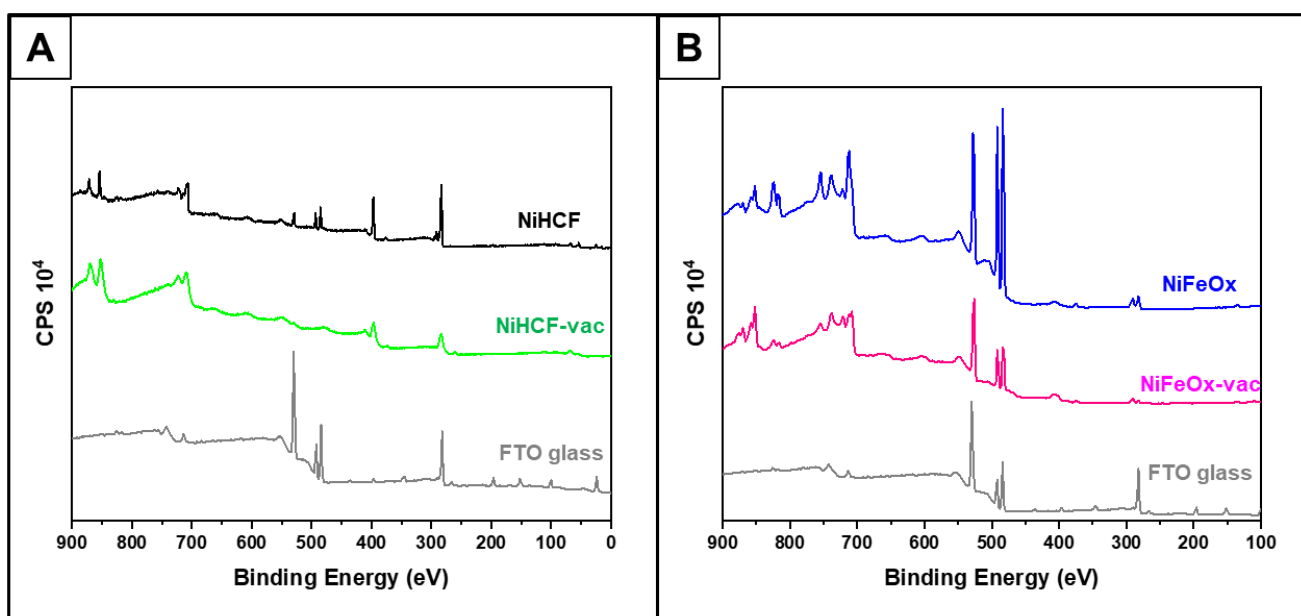


**Figure 26:** Soft X-ray photoelectron spectra of FTO glass, NiHCF and NiHCF-vac in pale-grey, black and green lines (A). FTO glass, NiFeOx and NiFeOx-vac in pale-grey, blue and pink lines (B).

**Table 6:** Atomic composition (At %) of Ni, Fe, N, and C elements in NiHCF and NiHCF-vac samples. Using the software CasaXPS© to fitting Area, Composition and peak attribution.

Elements	NiHCF	NiHCF-vac
	At %	
Ni	35.46	41.94
Fe	30.39	38.39
N	15.29	9.83
C	18.87	9.85

Another information we obtained is regarding the electronic binding energy shift in which Ni 2p and Fe 2p, N 1s and C 1s of NiHCF and NiHCF-vac were analyzed (Figure 28) as theoretically reported. For NiHCF, the binding energies for Ni 2p<sub>3/2</sub> and Ni 2p<sub>1/2</sub> are found to be 854.1 eV and 871.6 eV having an offset value from the theoretical (852.7 eV and 870.0 eV) of 1.4 eV and 1.6 eV. As for NiHCF-vac, the energies are found at 853.1 eV and 870.1 eV having a displacement value of 0.4 eV and 0.1 eV. For Fe 2p<sub>3/2</sub> and Fe 2p<sub>1/2</sub> (706.8 eV and 719.9 eV), binding energies are found for NiHCF to be 708.6 eV and 722.6 eV and for NiHCF-vac to be 709.1 eV and 723.1 eV, respectively. The shift variation is 1.8 eV and 2.7 eV for NiHCF while the shift is 2.3 eV and 3.2 eV for NiHCF-vac. Therefore, this difference may be related to the insertion of defect engineering into the sample, or also to the loading of samples during analysis.

For the analogues that underwent thermal treatment (Figure 26B) the survey profile is very similar, we can see the absence of N 1s and C 1s peaks in both samples, indicating that the cyanometallate structure of the material decomposed into oxides<sup>9</sup>, as the Ni 2p, Fe 2p, and O 1s peaks are noticeable in both samples, although there is substrate intensity contribution in the O 1s peak and Sn 3s (884 eV), 3p (750 ~ 715 eV) and 3d (493 ~ 484 eV) are more noticeable in the materials.

#### 4.7.2 X-ray absorbance spectroscopy

Additionally, synchrotron-based soft X-ray absorption spectroscopy (XAS), performed at the same IPÉ beamline station, was used to examine the ligand field structure, defects, and chemical speciation of Ni and Fe in the materials before and after catalysis for the water oxidation reaction seen from the differences in the electronic binding energy of Ni 2p and Fe 2p found by the results of the XPS survey<sup>7,43</sup>. The analyses were carried out using two types of detection methods: total electron yield (TEY), a more surface-sensitive method, and fluorescence yield (FY), which provides more bulk information about the samples in which the L<sub>3</sub> and L<sub>2</sub> edges (L<sub>3</sub> are 2p<sub>3/2</sub> and L<sub>2</sub> are 2p<sub>1/2</sub>) of Ni and Fe before and after catalysis were examined and the results are shown in Figure 27.

Analyzing the L<sub>3</sub> edge of Fe for NiHCF and NiHCF-vac (red and pink line), the L<sub>3</sub> have four resonant absorptions in the shoulder at 708.1 eV and the peak at 708.5 eV are assigned to Fe 2p<sub>3/2</sub> → Fe (3d t<sub>2g</sub>) and Fe 2p<sub>3/2</sub> → Fe (3d e<sub>g</sub>), respectively. The peak at 710.4 eV is Fe 2p<sub>3/2</sub> → π\* and the peak at 712.6 eV is attributed to Fe 2p<sub>3/2</sub> → σ\*<sup>44-47</sup>.

at the Fe L-edge (red line), it is possible to see in NiHCF that the pre-catalysis material has more  $\text{Fe}^{3+}$  in its structure, and post-catalysis, the intensity decreases, revealing more  $\text{Fe}^{2+}$  species in its structure and for NiHCF-vac, both before and after catalysis, there are more  $\text{Fe}^{3+}$  species in its structure, which is a notable difference compared to the analogue without defects, which has a significant portion of  $\text{Fe}^{2+}$  species in its structure.<sup>48–50</sup> We observe a small shift of the signals towards lower energy pre-catalysts values in NiHCF-vac surface (TEY), which suggests the replacement of cyanide to water ligand.

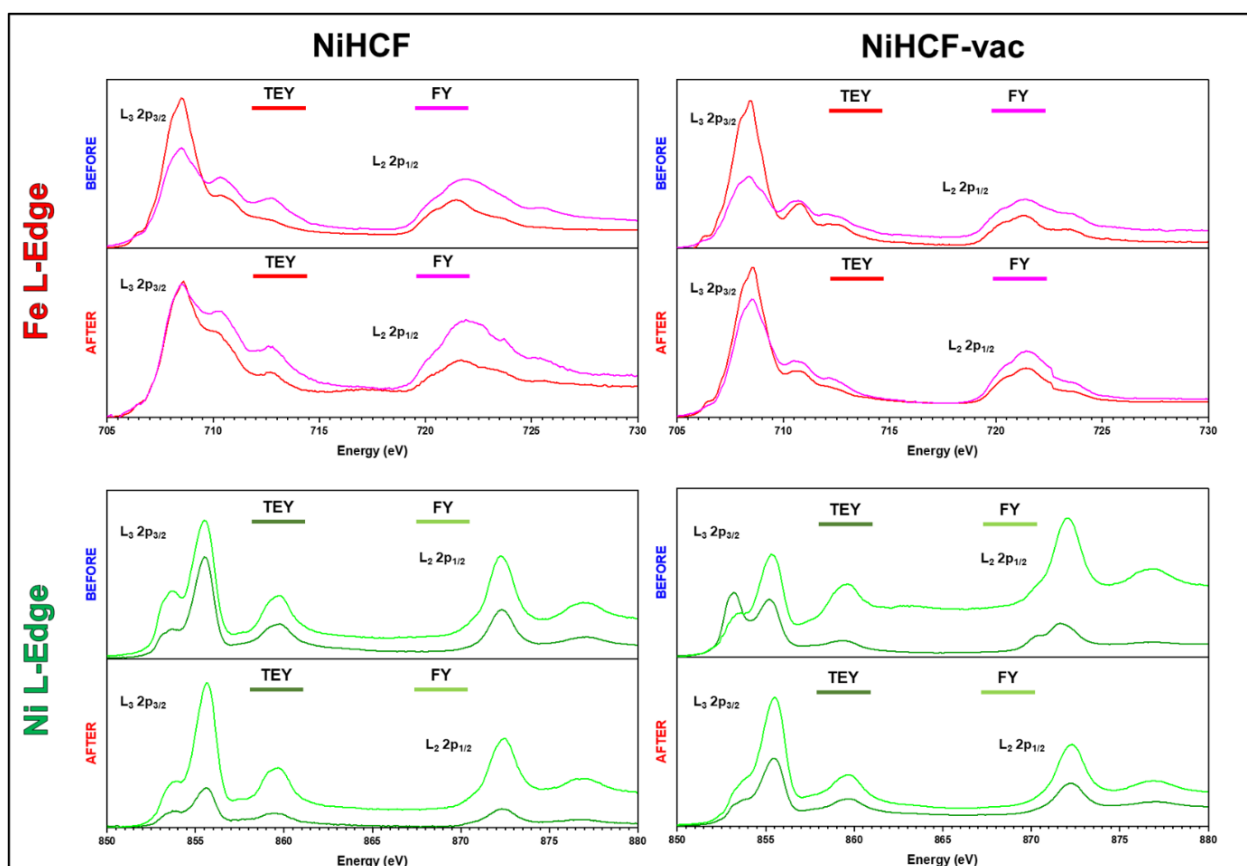


**Figure 27:** Soft X-ray absorption spectra for Fe and Ni  $L_{3,2}$  edges in NiHCF and NiHCF-vac before and after catalysis under mild conditions. Total electron yield (TEY) surface analysis and fluorescent yield (FY) bulk analysis.

For the  $L_3$  edge of Ni for NiHCF a NiHCF-vac (dark-green and green line), presents three resonant absorptions a shoulder at 853.5 eV, a peak 855.5 and a peak at 859.8 eV which are assigned to  $\text{Ni } 2p_{3/2} \rightarrow \text{Ni } (3d t_{2g})$  with a change of symmetry distortion of from Octahedral ( $O_h$ ) to pyramidal ( $C_{4v}$ ),  $\text{Ni } 2p_{3/2} \rightarrow \text{Ni } (3d e_g)$  and satellite peak respectively<sup>45,51–53</sup>. Moreover, at the Ni L-edge (green line), it is evident that the element is essentially in a  $\text{Ni}^{2+}$  low-spin (LS) configuration in NiHCF surface (TEY)<sup>45,54,55</sup>, while in NiHCF-vac the Ni L-edge, the nickel species are in a  $\text{Ni}^{2+}$  configuration pre-catalysis it is in a high-spin state (HS), while post-catalysis, it returns

to a low-spin state in surface (TEY). The high-spin configuration of Ni<sup>2+</sup> species pre-catalysis might indicate a symmetry distortion implied in an improved catalytic performance due to the introduction of defect engineering in the structure<sup>56-58</sup>, or another hypothesis for these differences in NiHCF-vac Ni L-edge surface (TEY) is the formation of the NiOOH in the surface in which it labilizes during catalysis<sup>51</sup>. We observe a small shift of the signals towards lower energy values in NiHCF-vac, which suggests the replacement of cyanide to water ligand and the values are tabled below.

**Table 7:** Surface analysis (TEY) before and after catalysis differences in Ni and Fe L<sub>3,2</sub> edges in NiHCF, NiHCF-vac and NiFeOx.

TEY analysis	Fe L-Edge				Ni L-Edge			
	L3 (2p <sub>3/2</sub> )	L2 (2p <sub>1/2</sub> )	L3 (2p <sub>3/2</sub> )	L2 (2p <sub>1/2</sub> )	L3 (2p <sub>3/2</sub> )	L2 (2p <sub>1/2</sub> )	L3 (2p <sub>3/2</sub> )	L2 (2p <sub>1/2</sub> )
	Before		After		Before		After	
NiHCF	708.5 – 710.5 – 712.7	720.4 – 721.5 – 723.6	708.6 – 710.2 – 712.6	720.6 – 721.6 – 723.4	853.6 – 855.5	872.3 – 877.1	853.7 – 855.6	872.3 – 876.8
NiHCF-vac	708.4 – 710.7 – 712.3	720.4 – 721.3 – 723.5	708.5 – 710.6 – 712.4	720.4 – 721.4 – 723.4	853.2 – 855.2	870.4 – 871.6	853.6 – 855.4	872.2 – 876.9
NiFeOx	708.6 – 710.1	721.7 – 723.3	708.6 – 710.1	721.6 – 723.4	853.4 – 855.3	870.6 – 871.7	853.4 – 855.2	870.5 – 871.6

When analyzing the materials that underwent thermal treatment compared to NiHCF (Figure 28), it is noticeable that both Fe and Ni at the L-edge are predominantly in the Fe<sup>3+</sup> (red line) and Ni<sup>2+</sup> (green line) oxidation states, respectively, and they are in a high-spin (HS) configuration both pre-and post-catalysis<sup>56,58</sup>. This is a strong indication of why the nickel Prussian blue analogues that underwent thermal treatment exhibit better performance as catalysts for the water oxidation reaction compared with their precursor. Further investigations will be carried out in the literature to confirm our proposed hypotheses based on the results obtained at the national synchrotron light laboratory (LNLS).

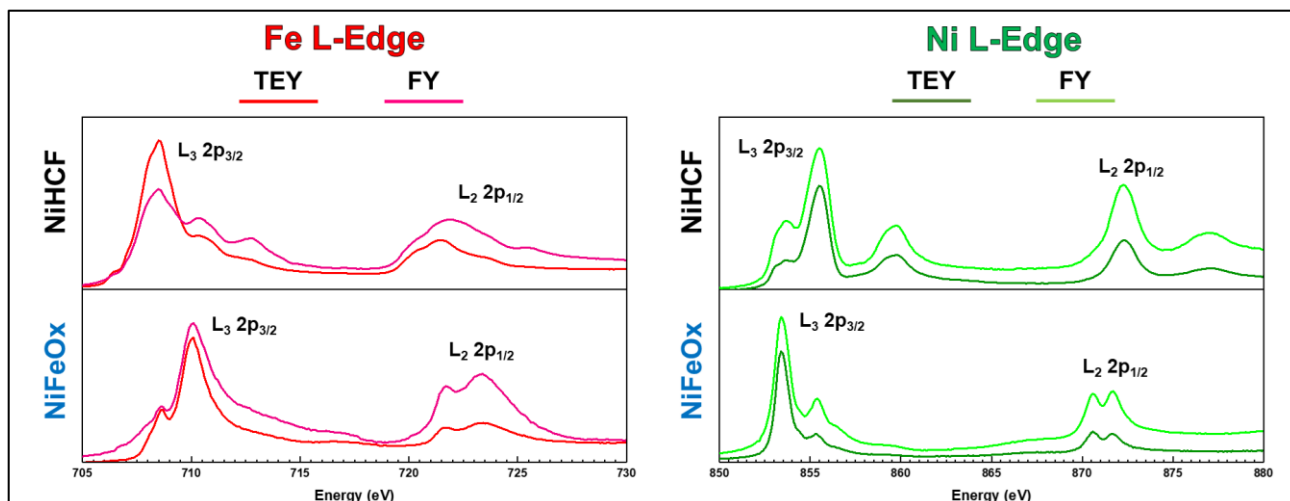


**Figure 28:** Soft X-ray absorption spectra for Fe and Ni  $L_{3,2}$  edges in NiHCF and NiFeOx before the catalysts under mild conditions. Total electron yield (TEY) surface analysis and fluorescent yield (FY) bulk analysis.

## 5. CONCLUSION

In conclusion, it was possible to electrochemically synthesize nickel Prussian blue analogue on the FTO glass substrate and use it as a template to produce metal oxides for its use as catalysts in the water oxidation reaction. Additionally, defect engineering was implemented in its structure through an electrochemical process, and its verification and implications were analyzed and evaluated using spectroscopic, microscopic, and electrochemical techniques. A catalytic study of all synthesized catalysts was conducted, comparing them to  $\text{RuO}_2$  for the water oxidation reaction under mild conditions based on Tafel slope. Although none of the evaluated samples presented a Tafel value lower than  $\text{RuO}_2$ , the implementation of defects and thermal treatment reduced this value compared to the analogue without any of these processes, positively impacting its electrocatalytic performance under neutral conditions. The results demonstrate a catalytic improvement in charge transfer ( $R_{ct}$ ) from  $234 \Omega$  to  $63.6 \Omega$  and  $18.9 \Omega$ , a decrease in the overpotential ( $\eta$ ) from  $821 \text{ mV}$  to  $774 \text{ mV}$  and  $740 \text{ mV}$  for NiHCF, NiHCF-vac, and NiFeOx, respectively. Furthermore, the use of synchrotron light allowed for the verification of the chemical speciation and oxidation states of the metals in the catalysts using synchrotron soft X-ray techniques. Although the work can predict that defect engineering improves the performance of catalysts for the water oxidation reaction, there are still many challenges regarding how it influences the reaction mechanism of water electrolysis.

## REFERENCES

- (1) Data, O. W. in; Roser, M. OWID Homepage. *Our World in Data* **2024**.
- (2) Von Zuben, T.; Moreira, D.; Germscheidt, R.; Yoshimura, R.; Dorretto, D.; de Araujo, A.; Salles Jr., A.; Bonacin, J. Is Hydrogen Indispensable for a Sustainable World? A Review of H<sub>2</sub> Applications and Perspectives for the Next Years. *J. Braz. Chem. Soc.* **2022**. <https://doi.org/10.21577/0103-5053.20220026>.
- (3) Germscheidt, R. L.; Moreira, D. E. B.; Yoshimura, R. G.; Gasbarro, N. P.; Datti, E.; dos Santos, P. L.; Bonacin, J. A. Hydrogen Environmental Benefits Depend on the Way of Production: An Overview of the Main Processes Production and Challenges by 2050. *Adv Energy Sustain Res* **2021**, 2 (10), 2100093. <https://doi.org/10.1002/aesr.202100093>.
- (4) Megía, P. J.; Vizcaíno, A. J.; Calles, J. A.; Carrero, A. Hydrogen Production Technologies: From Fossil Fuels toward Renewable Sources. A Mini Review. *Energy Fuels* **2021**, 35 (20), 16403–16415. <https://doi.org/10.1021/acs.energyfuels.1c02501>.
- (5) Sharifian, R.; Wagterveld, R. M.; Digdaya, I. A.; Xiang, C.; Vermaas, D. A. Electrochemical Carbon Dioxide Capture to Close the Carbon Cycle. *Energy Environ. Sci.* **2021**, 14 (2), 781–814. <https://doi.org/10.1039/D0EE03382K>.
- (6) Zambiasi, P. J.; Aparecido, G. de O.; Ferraz, T. V. de B.; Skinner, W. S. J.; Yoshimura, R. G.; Moreira, D. E. B.; Germscheidt, R. L.; Nascimento, L. L.; Patrocínio, A. O. T.; Formiga, A. L. B.; Bonacin, J. A. Electrocatalytic Water Oxidation Reaction Promoted by Cobalt-Prussian Blue and Its Thermal Decomposition Product under Mild Conditions. *Dalton Trans.* **2020**, 49 (45), 16488–16497. <https://doi.org/10.1039/D0DT02220A>.
- (7) Germscheidt, R. L.; da Silva Francischini, D.; Silva, M. B.; Zezzi Arruda, M. A.; Barboza Formiga, A. L.; Rizuti da Rocha, T. C.; Bonacin, J. A. Water Oxidation Performance Enhanced by Electrochemically Designed Vacancies on a Prussian Blue Catalyst. *ACS Appl. Energy Mater.* **2022**, 5 (8), 9447–9454. <https://doi.org/10.1021/acsaem.2c00994>.
- (8) Xiong, Y.; He, P. A Review on Electrocatalysis for Alkaline Oxygen Evolution Reaction (OER) by Fe-Based Catalysts. *J Mater Sci* **2023**, 58 (5), 2041–2067. <https://doi.org/10.1007/s10853-023-08176-1>.
- (9) McCrory, C. C. L.; Jung, S.; Peters, J. C.; Jaramillo, T. F. Benchmarking Heterogeneous Electrocatalysts for the Oxygen Evolution Reaction. *J. Am. Chem. Soc.* **2013**, 135 (45), 16977–16987. <https://doi.org/10.1021/ja407115p>.
- (10) McCrory, C. C. L.; Jung, S.; Ferrer, I. M.; Chatman, S. M.; Peters, J. C.; Jaramillo, T. F. Benchmarking Hydrogen Evolving Reaction and Oxygen Evolving Reaction Electrocatalysts for Solar Water Splitting Devices. *J. Am. Chem. Soc.* **2015**, 137 (13), 4347–4357. <https://doi.org/10.1021/ja510442p>.
- (11) El-Shafie, M. Hydrogen Production by Water Electrolysis Technologies: A Review. *Results in Engineering* **2023**, 20, 101426. <https://doi.org/10.1016/j.rineng.2023.101426>.
- (12) Doyle, R. L.; Lyons, M. E. G. The Oxygen Evolution Reaction: Mechanistic Concepts and Catalyst Design. In *Photoelectrochemical Solar Fuel Production*; Giménez, S., Bisquert, J., Eds.; Springer International Publishing: Cham, 2016; pp 41–104. [https://doi.org/10.1007/978-3-319-29641-8\\_2](https://doi.org/10.1007/978-3-319-29641-8_2).
- (13) Alsaç, E. P.; Ülker, E.; Nune, S. V. K.; Dede, Y.; Karadas, F. Tuning the Electronic Properties of Prussian Blue Analogues for Efficient Water Oxidation Electrocatalysis: Experimental and Computational Studies. *Chem. Eur. J.* **2018**, 24 (19), 4856–4863. <https://doi.org/10.1002/chem.201704933>.
- (14) Lee, J. H.; Kattel, S.; Wang, Y.; Tackett, B. M.; Xie, Z.; Hwang, S.; Denny, S. R.; Xu, W.; Chen, J. G. Prussian Blue Analogues as Platform Materials for Understanding and Developing Oxygen Evolution Reaction Electrocatalysts. *Journal of Catalysis* **2021**, 393, 390–398. <https://doi.org/10.1016/j.jcat.2020.12.002>.

- (15) Lei, L.; Huang, D.; Cheng, M.; Deng, R.; Chen, S.; Chen, Y.; Wang, W. Defects Engineering of Bimetallic Ni-Based Catalysts for Electrochemical Energy Conversion. *Coordination Chemistry Reviews* **2020**, *418*, 213372. <https://doi.org/10.1016/j.ccr.2020.213372>.
- (16) Avila, Y.; Acevedo-Peña, P.; Reguera, L.; Reguera, E. Recent Progress in Transition Metal Hexacyanometallates: From Structure to Properties and Functionality. *Coordination Chemistry Reviews* **2022**, *453*, 214274. <https://doi.org/10.1016/j.ccr.2021.214274>.
- (17) Yu, Z.-Y.; Duan, Y.; Liu, J.-D.; Chen, Y.; Liu, X.-K.; Liu, W.; Ma, T.; Li, Y.; Zheng, X.-S.; Yao, T.; Gao, M.-R.; Zhu, J.-F.; Ye, B.-J.; Yu, S.-H. Unconventional CN Vacancies Suppress Iron-Leaching in Prussian Blue Analogue Pre-Catalyst for Boosted Oxygen Evolution Catalysis. *Nat Commun* **2019**, *10* (1), 2799. <https://doi.org/10.1038/s41467-019-10698-9>.
- (18) Deng, W.; Xu, B.; Zhao, Q.; Xie, S.; Jin, W.; Zhang, X.; Gao, B.; Liu, Z.; Abd-Allah, Z.; Chu, P. K.; Peng, X. C≡N Vacancy Engineering of Prussian Blue Analogs for the Advanced Oxygen Evolution Reaction. *Journal of Environmental Chemical Engineering* **2023**, *11* (2), 109407. <https://doi.org/10.1016/j.jece.2023.109407>.
- (19) Bornamehr, B.; Presser, V.; Zarbin, A. J. G.; Yamauchi, Y.; Husmann, S. Prussian Blue and Its Analogues as Functional Template Materials: Control of Derived Structure Compositions and Morphologies. *J. Mater. Chem. A* **2023**, *11* (20), 10473–10492. <https://doi.org/10.1039/D2TA09501G>.
- (20) Kibsgaard, J.; Hellstern, T. R.; Choi, S.-J.; Reinecke, B. N.; Jaramillo, T. F. Mesoporous Ruthenium/Ruthenium Oxide Thin Films: Active Electrocatalysts for the Oxygen Evolution Reaction. *ChemElectroChem* **2017**, *4* (10), 2480–2485. <https://doi.org/10.1002/celec.201700334>.
- (21) Huang, J.; Hou, M.; Wang, J.; Teng, X.; Niu, Y.; Xu, M.; Chen, Z. RuO<sub>2</sub> Nanoparticles Decorate Belt-like Anatase TiO<sub>2</sub> for Highly Efficient Chlorine Evolution. *Electrochimica Acta* **2020**, *339*, 135878. <https://doi.org/10.1016/j.electacta.2020.135878>.
- (22) Rossi, T. S.; Tenório, L. N.; Guedes-Sobrinho, D.; Winnischofer, H.; Vidotti, M. Influence of Electrosynthesis Methods in the Electrocatalytical and Morphological Properties of Cobalt and Nickel Hexacyanoferrate Films. *Electrochimica Acta* **2020**, *361*, 137021. <https://doi.org/10.1016/j.electacta.2020.137021>.
- (23) Bayzi Isfahani, V.; Arab, A.; Horta Belo, J.; Pedro Araújo, J.; Manuela Silva, M.; Gonçalves Almeida, B. Comparison of Physical/Chemical Properties of Prussian Blue Thin Films Prepared by Different Pulse and DC Electrodeposition Methods. *Materials* **2022**, *15* (24), 8857. <https://doi.org/10.3390/ma15248857>.
- (24) Karupppasamy, K.; Bose, R.; Velusamy, D. B.; Vikraman, D.; Santhoshkumar, P.; Sivakumar, P.; Alfantazi, A.; Kim, H.-S. Rational Design and Engineering of Metal–Organic Framework-Derived Trimetallic NiCoFe-Layered Double Hydroxides as Efficient Electrocatalysts for Water Oxidation Reaction. *ACS Sustainable Chem. Eng.* **2022**, *10* (45), 14693–14704. <https://doi.org/10.1021/acssuschemeng.2c02830>.
- (25) Han, L.; Tang, P.; Reyes-Carmona, Á.; Rodríguez-García, B.; Torrén, M.; Morante, J. R.; Arbiol, J.; Galan-Mascaros, J. R. Enhanced Activity and Acid pH Stability of Prussian Blue-Type Oxygen Evolution Electrocatalysts Processed by Chemical Etching. *J. Am. Chem. Soc.* **2016**, *138* (49), 16037–16045. <https://doi.org/10.1021/jacs.6b09778>.
- (26) Craig, M. J.; Coulter, G.; Dolan, E.; Soriano-López, J.; Mates-Torres, E.; Schmitt, W.; García-Melchor, M. Universal Scaling Relations for the Rational Design of Molecular Water Oxidation Catalysts with Near-Zero Overpotential. *Nat Commun* **2019**, *10* (1), 4993. <https://doi.org/10.1038/s41467-019-12994-w>.

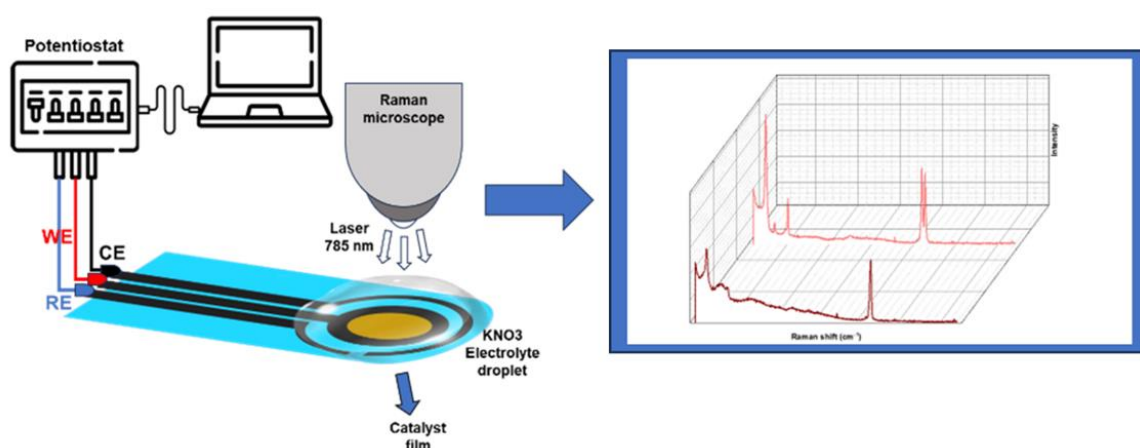
- (27) Zambiazzi, P.; de Moraes, A.; Kogachi, R.; Aparecido, G.; Formiga, A.; Bonacin, J. Performance of Water Oxidation by 3D Printed Electrodes Modified by Prussian Blue Analogues. *J. Braz. Chem. Soc.* **2020**. <https://doi.org/10.21577/0103-5053.20200088>.
- (28) Lehto, J.; Haukka, S.; Koskinen, P.; Blomberg, M. Thermal Decomposition of Potassium Cobalt Hexacyanoferrate(II). *Thermochimica Acta* **1990**, *160* (2), 343–347. [https://doi.org/10.1016/0040-6031\(90\)80275-4](https://doi.org/10.1016/0040-6031(90)80275-4).
- (29) de Tacconi, N. R.; Rajeshwar, K.; Lezna, R. O. Metal Hexacyanoferrates: Electrosynthesis, in Situ Characterization, and Applications. *Chem. Mater.* **2003**, *15* (16), 3046–3062. <https://doi.org/10.1021/cm0341540>.
- (30) Pyrasch, M.; Toutianoush, A.; Jin, W.; Schnepf, J.; Tieke, B. Self-Assembled Films of Prussian Blue and Analogues: Optical and Electrochemical Properties and Application as Ion-Sieving Membranes. *Chem. Mater.* **2003**, *15* (1), 245–254. <https://doi.org/10.1021/cm021230a>.
- (31) Gotoh, A.; Uchida, H.; Ishizaki, M.; Satoh, T.; Kaga, S.; Okamoto, S.; Ohta, M.; Sakamoto, M.; Kawamoto, T.; Tanaka, H.; Tokumoto, M.; Hara, S.; Shiozaki, H.; Yamada, M.; Miyake, M.; Kurihara, M. Simple Synthesis of Three Primary Colour Nanoparticle Inks of Prussian Blue and Its Analogues. *Nanotechnology* **2007**, *18* (34), 345609. <https://doi.org/10.1088/0957-4484/18/34/345609>.
- (32) Wang, H.; Zhou, S.; Wang, Z.; Xu, S.; Dong, S.; Miao, Y. Electrochemical Conversion of Ni(OH)<sub>2</sub> Nanoparticle Film into Nickel Hexacyanoferrate through a Simple Strategy of Potential Cycling. *Electrochimica Acta* **2012**, *74*, 201–206. <https://doi.org/10.1016/j.electacta.2012.04.059>.
- (33) Toma, H. E.; Bonifácio, L. da S.; Anaissi, F. J. Da cor à cor inexistente: uma reflexão sobre espectros eletrônicos e efeitos cromáticos. *Quím. Nova* **2005**, *28*, 897–900. <https://doi.org/10.1590/S0100-40422005000500030>.
- (34) Alexander, J. J.; Gray, H. B. Electronic Structures of Hexacyanometalate Complexes. *J. Am. Chem. Soc.* **1968**, *90* (16), 4260–4271. <https://doi.org/10.1021/ja01018a013>.
- (35) Gushikem, Y. Espectros eletrônicos de alguns complexos de geometria octaédrica de Ni<sup>2+</sup>: uma introdução prática à teoria do campo cristalino no curso de graduação. *Quím. Nova* **2005**, *28*, 153–156. <https://doi.org/10.1590/S0100-40422005000100027>.
- (36) Sefhra, P. J.; Baraneedharan, P.; Sivakumar, M.; Thangaian, D. T.; Nehru, K. In Situ Growth of Hexagonal-Shaped  $\alpha$ -Fe<sub>2</sub>O<sub>3</sub> Nanostructures over Few Layered Graphene by Hydrothermal Method and Their Electrochemical Performance. *Journal of Materials Science. Materials in Electronics* **2018**, 1–11. <https://doi.org/10.1007/s10854-018-8676-1>.
- (37) Gandhi, A. C.; Cheng, H.-Y.; Chang, Y.-M.; Lin, J. G. Size Confined Magnetic Phase in NiO Nanoparticles. *Mater. Res. Express* **2016**, *3* (3), 035017. <https://doi.org/10.1088/2053-1591/3/3/035017>.
- (38) Ahlawat, A.; Sathe, V. G. Raman Study of NiFe<sub>2</sub>O<sub>4</sub> Nanoparticles, Bulk and Films: Effect of Laser Power. *Journal of Raman Spectroscopy* **2011**, *42* (5), 1087–1094. <https://doi.org/10.1002/jrs.2791>.
- (39) Vázquez-Samperio, J.; Sánchez-Padilla, N. M.; Acevedo-Peña, P.; Cano, A.; Nava, N.; Morales-Acosta, D.; Oliver-Tolentino, M. Ni Prussian Blue Analogue/Mesoporous Carbon Composite as Electrode Material for Aqueous K-Ion Energy Storage: Effect of Carbon-Framework Interaction on Its Electrochemical Behavior. *ChemistrySelect* **2018**, *3* (41), 11441–11450. <https://doi.org/10.1002/slct.201801333>.
- (40) Eren, E.; Uygun Oksuz, A. Flexible Nickel Prussian Blue Analogue Films for Electrochromic and H<sub>2</sub>O<sub>2</sub> Sensing. *J Mater Sci: Mater Electron* **2020**, *31* (18), 15434–15445. <https://doi.org/10.1007/s10854-020-04106-y>.

- (41) Wei, L.; Zhang, Y.; Yang, Y.; Ye, M.; Li, C. In-Situ Activated NiFePBA-FeOOH Electrocatalyst for Oxygen Evolution Reaction and Zinc-Air Battery. *ChemistrySelect* **2021**, *6* (15), 3683–3691. <https://doi.org/10.1002/slct.202100911>.
- (42) Anantharaj, S.; Noda, S. Appropriate Use of Electrochemical Impedance Spectroscopy in Water Splitting Electrocatalysis. *ChemElectroChem* **2020**, *7* (10), 2297–2308. <https://doi.org/10.1002/celec.202000515>.
- (43) Wu, B.; Sun, T.; You, Y.; Meng, H.; Morales, D. M.; Lounasvuori, M.; Beheshti Askari, A.; Jiang, L.; Zeng, F.; Hu, B.; Zhang, X.; Tai, R.; Xu, Z. J.; Petit, T.; Mai, L. In Situ X-Ray Absorption Spectroscopy of Metal/Nitrogen-Doped Carbons in Oxygen Electrocatalysis. *Angewandte Chemie International Edition n/a* (n/a), e202219188. <https://doi.org/10.1002/anie.202219188>.
- (44) Engel, N.; Bokarev, S. I.; Suljoti, E.; Garcia-Diez, R.; Lange, K. M.; Atak, K.; Golnak, R.; Kothe, A.; Dantz, M.; Kühn, O.; Aziz, E. F. Chemical Bonding in Aqueous Ferrocyanide: Experimental and Theoretical X-Ray Spectroscopic Study. *J. Phys. Chem. B* **2014**, *118* (6), 1555–1563. <https://doi.org/10.1021/jp411782y>.
- (45) Arrio, M.-A.; Saintavit, Ph.; Cartier dit Moulin, Ch.; Mallah, T.; Verdaguer, M.; Pellegrin, E.; Chen, C. T. Characterization of Chemical Bonds in Bimetallic Cyanides Using X-Ray Absorption Spectroscopy at L2,3 Edges. *J. Am. Chem. Soc.* **1996**, *118* (27), 6422–6427. <https://doi.org/10.1021/ja9542698>.
- (46) Cartier Dit Moulin, C.; Villain, F.; Bleuzen, A.; Arrio, M.-A.; Saintavit, P.; Lomenech, C.; Escax, V.; Baudelet, F.; Dartyge, E.; Gallet, J.-J.; Verdaguer, M. Photoinduced Ferrimagnetic Systems in Prussian Blue Analogues  $C^I_x Co_4 [Fe(CN)_6]_y$  ( $C^I =$  Alkali Cation). 2. X-Ray Absorption Spectroscopy of the Metastable State. *J. Am. Chem. Soc.* **2000**, *122* (28), 6653–6658. <https://doi.org/10.1021/ja000349m>.
- (47) Hocking, R. K.; Wasinger, E. C.; De Groot, F. M. F.; Hodgson, K. O.; Hedman, B.; Solomon, E. I. Fe L-Edge XAS Studies of  $K_4 [Fe(CN)_6]$  and  $K_3 [Fe(CN)_6]$ : A Direct Probe of Back-Bonding. *J. Am. Chem. Soc.* **2006**, *128* (32), 10442–10451. <https://doi.org/10.1021/ja061802i>.
- (48) Lee, E.; Kim, D. H.; Hwang, J.; Kang, J.-S.; Van Minh, N.; Yang, I.-S.; Ueno, T.; Sawada, M. Soft X-Ray Absorption Spectroscopy Study of Prussian Blue Analogue  $ACo[Fe(CN)_6]H_2O$  Nano-Particles (A=Na, K). *Journal of the Korean Physical Society* **2013**, *62* (12), 1910–1913. <https://doi.org/10.3938/jkps.62.1910>.
- (49) Dumas, T.; Guillaumont, D.; Moisy, P.; Shuh, D. K.; Tyliszczak, T.; Solari, P. L.; Den Auwer, C. The Electronic Structure of F-Element Prussian Blue Analogs Determined by Soft X-Ray Absorption Spectroscopy. *Chem. Commun.* **2018**, *54* (86), 12206–12209. <https://doi.org/10.1039/C8CC05176C>.
- (50) Kudo, K.; Takeshita, R.; Kobayashi, D.; Iwazumi, T.; Tokoro, H.; Nakagawa, K.; Ohkoshi, S.; Kitajima, Y. Detailed Fe 3d Electronic Structures of Prussian Blue Analogs Studied by X-Ray Absorption Spectroscopy. *Materials Today: Proceedings* **2023**, S2214785323021818. <https://doi.org/10.1016/j.matpr.2023.04.280>.
- (51) Takada, N.; Uchiyama, T.; Uchimoto, Y.; Yamagishi, H.; Ohta, T.; Orikasa, Y. Soft X-Ray Absorption Spectroscopic Study on Nickel Electrode for Alkaline Water Electrolysis. **2019**, No. 21.
- (52) Wang, H.; Ralston, C. Y.; Patil, D. S.; Jones, R. M.; Gu, W.; Verhagen, M.; Adams, M.; Ge, P.; Riordan, C.; Marganian, C. A.; Mascharak, P.; Kovacs, J.; Miller, C. G.; Collins, T. J.; Brooker, S.; Croucher, P. D.; Wang, K.; Stiefel, E. I.; Cramer, S. P. Nickel L-Edge Soft X-Ray Spectroscopy of Nickel–Iron Hydrogenases and Model Compounds Evidence for High-Spin Nickel(II) in the Active Enzyme. *J. Am. Chem. Soc.* **2000**, *122* (43), 10544–10552. <https://doi.org/10.1021/ja000945g>.

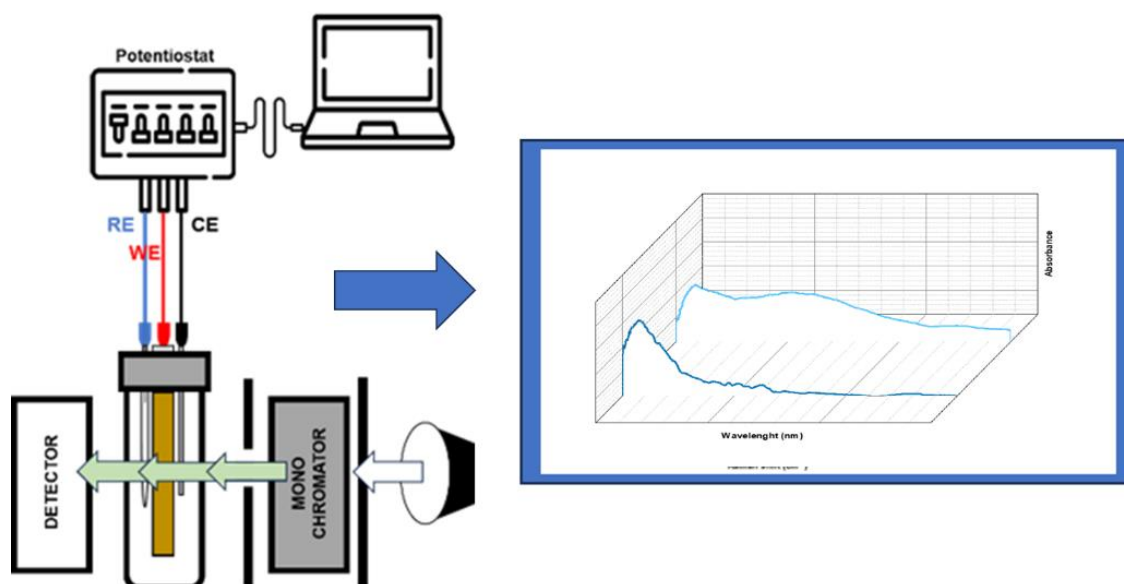
- (53) Wang, H.; Butorin, S. M.; Young, A. T.; Guo, J. Nickel Oxidation States and Spin States of Bioinorganic Complexes from Nickel L-Edge X-Ray Absorption and Resonant Inelastic X-Ray Scattering. *J. Phys. Chem. C* **2013**, *117* (47), 24767–24772. <https://doi.org/10.1021/jp402404b>.
- (54) Bonhommeau, S.; Pontius, N.; Cobo, S.; Salmon, L.; Groot, F. M. F. de; Molnár, G.; Bousseksou, A.; Dürr, H. A.; Eberhardt, W. Metal-to-Ligand and Ligand-to-Metal Charge Transfer in Thin Films of Prussian Blue Analogues Investigated by X-Ray Absorption Spectroscopy. *Phys. Chem. Chem. Phys.* **2008**, *10* (38), 5882–5889. <https://doi.org/10.1039/B806783J>.
- (55) Aguilà, D.; Prado, Y.; Koumoussi, E. S.; Mathonière, C.; Clérac, R. Switchable Fe/Co Prussian Blue Networks and Molecular Analogues. *Chem. Soc. Rev.* **2015**, *45* (1), 203–224. <https://doi.org/10.1039/C5CS00321K>.
- (56) Baker, M. L.; Mara, M. W.; Yan, J. J.; Hodgson, K. O.; Hedman, B.; Solomon, E. I. K- and L-Edge X-Ray Absorption Spectroscopy (XAS) and Resonant Inelastic X-Ray Scattering (RIXS) Determination of Differential Orbital Covalency (DOC) of Transition Metal Sites. *Coordination Chemistry Reviews* **2017**, *345*, 182–208. <https://doi.org/10.1016/j.ccr.2017.02.004>.
- (57) Timoshenko, J.; Roldan Cuenya, B. In Situ/Operando Electrocatalyst Characterization by X-Ray Absorption Spectroscopy. *Chem. Rev.* **2021**, *121* (2), 882–961. <https://doi.org/10.1021/acs.chemrev.0c00396>.
- (58) Risch, M.; Morales, D. M.; Villalobos, J.; Antipin, D. What X-Ray Absorption Spectroscopy Can Tell Us About the Active State of Earth-Abundant Electrocatalysts for the Oxygen Evolution Reaction\*\*. *Angew Chem Int Ed* **2022**, *61* (50). <https://doi.org/10.1002/anie.202211949>.
- (59) dos Santos, M. F.; Katic, V.; dos Santos, P. L.; Pires, B. M.; Formiga, A. L. B.; Bonacin, J. A. 3D-Printed Low-Cost Spectroelectrochemical Cell for In Situ Raman Measurements. *Anal. Chem.* **2019**, *91* (16), 10386–10389. <https://doi.org/10.1021/acs.analchem.9b01518>.

## APPENDIX

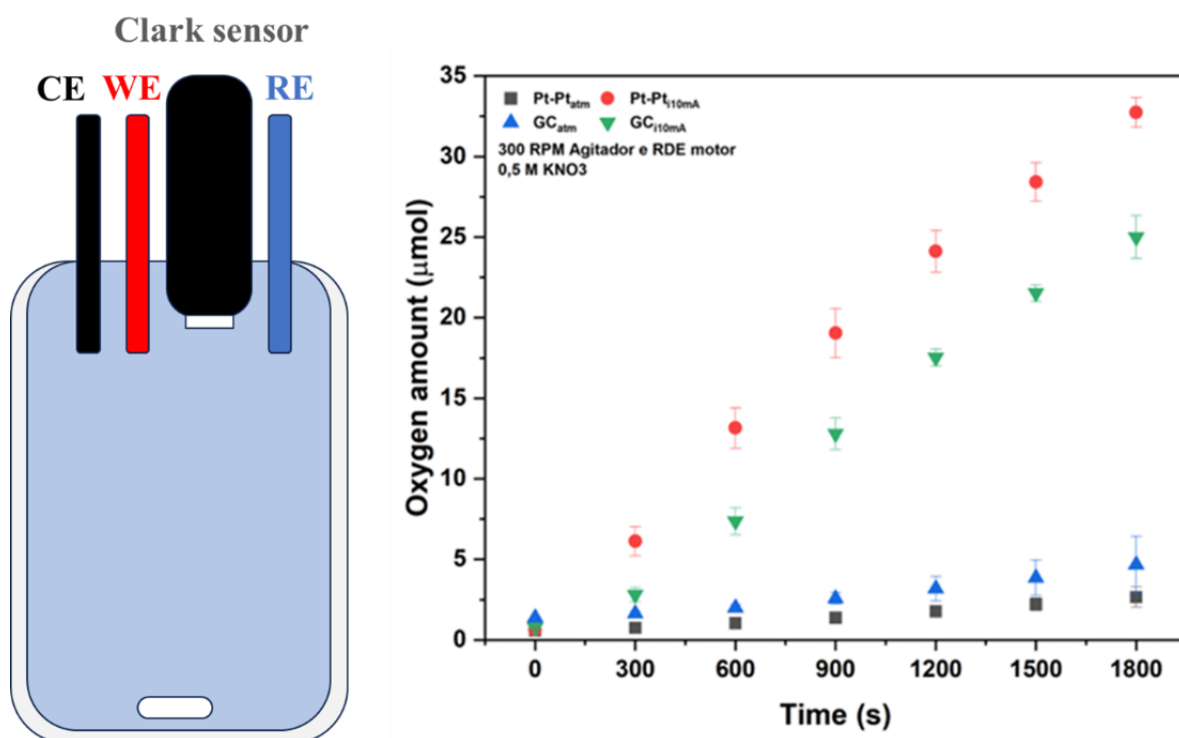
It is necessary to conduct some spectroscopic perform possible *in situ* tests (electrochemistry coupled with spectroscopy, see the schematic procedure in supplementary information S1 and S2<sup>29,59</sup> to enrich the discussion of the results obtained so far. Additionally, it is crucial to quantify the amount of oxygen gas produced with the prepared catalysts and determine whether the creation of defects and thermal treatment improve the amount of oxygen gas produced from the water-splitting reaction (see the schematic project in S3).



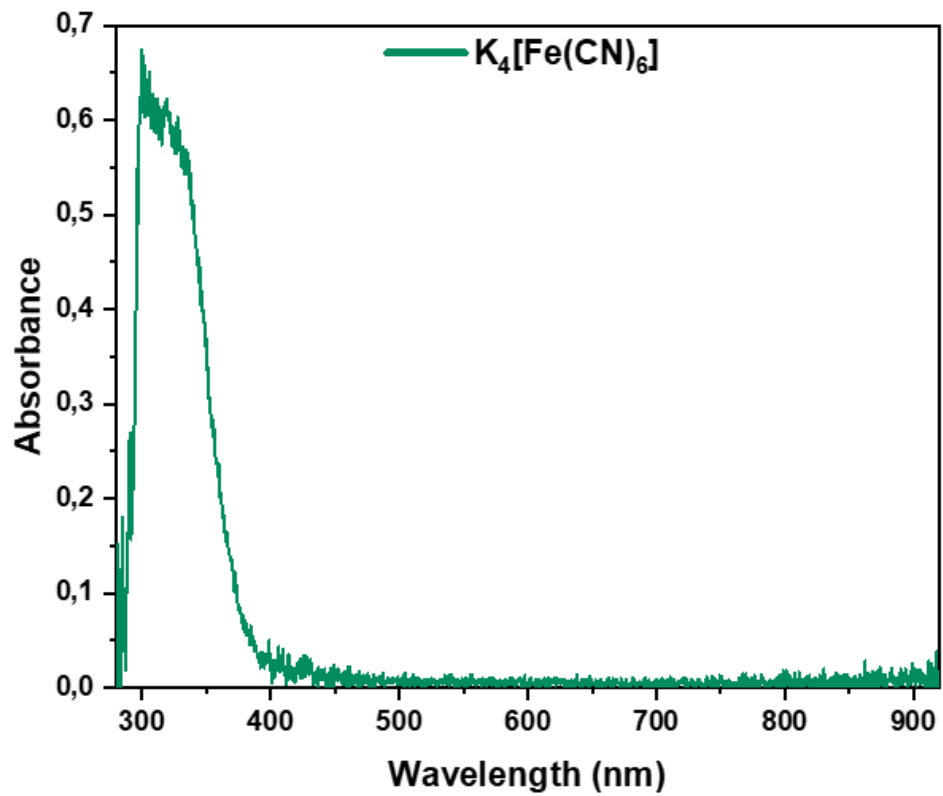
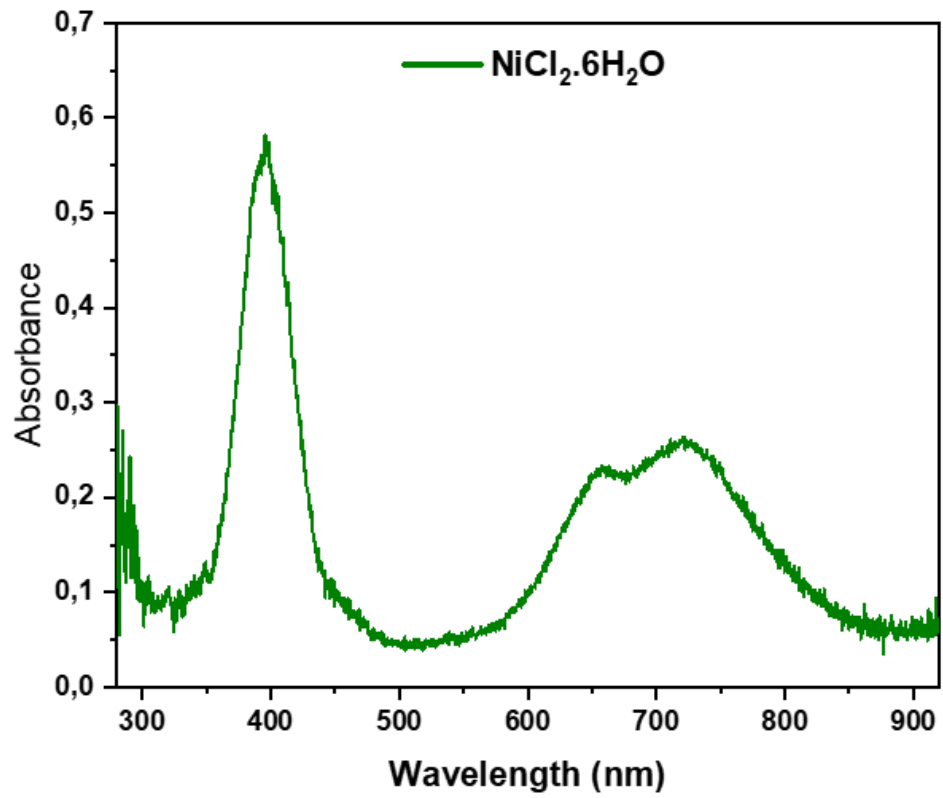
S1: Schematic Raman spectroscopy *in situ* study using a screen-printed carbon electrode in a droplet electrolyte.

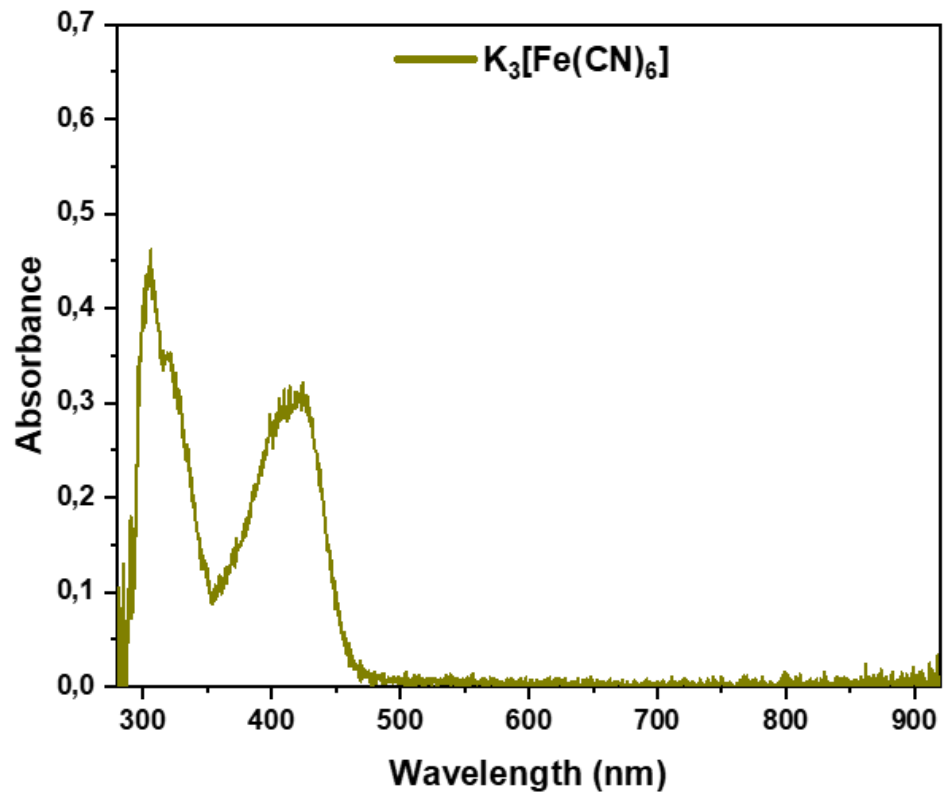


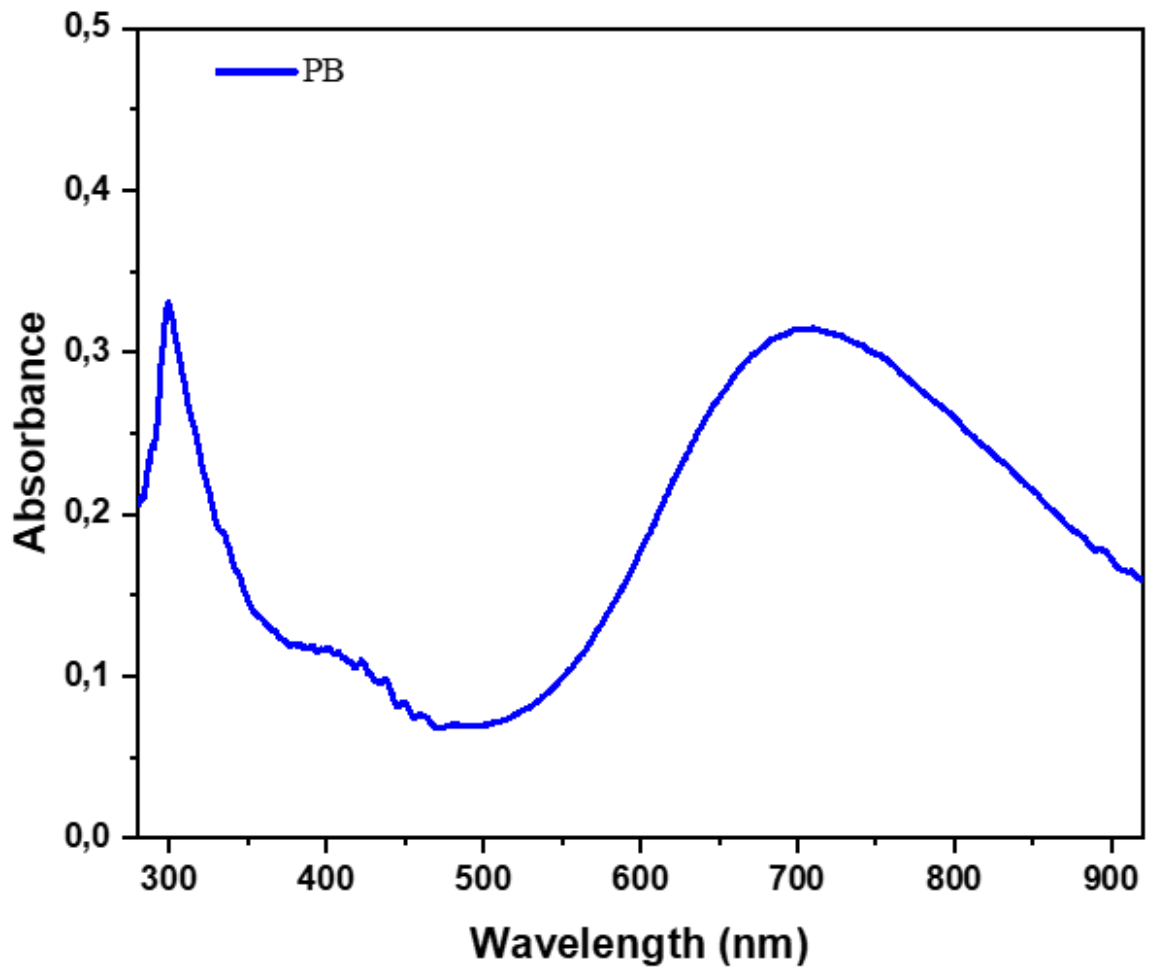
S2: Schematic electronic UV-visible spectroscopy *in situ* study using a miniaturized electrochemical cell as a cuvette.

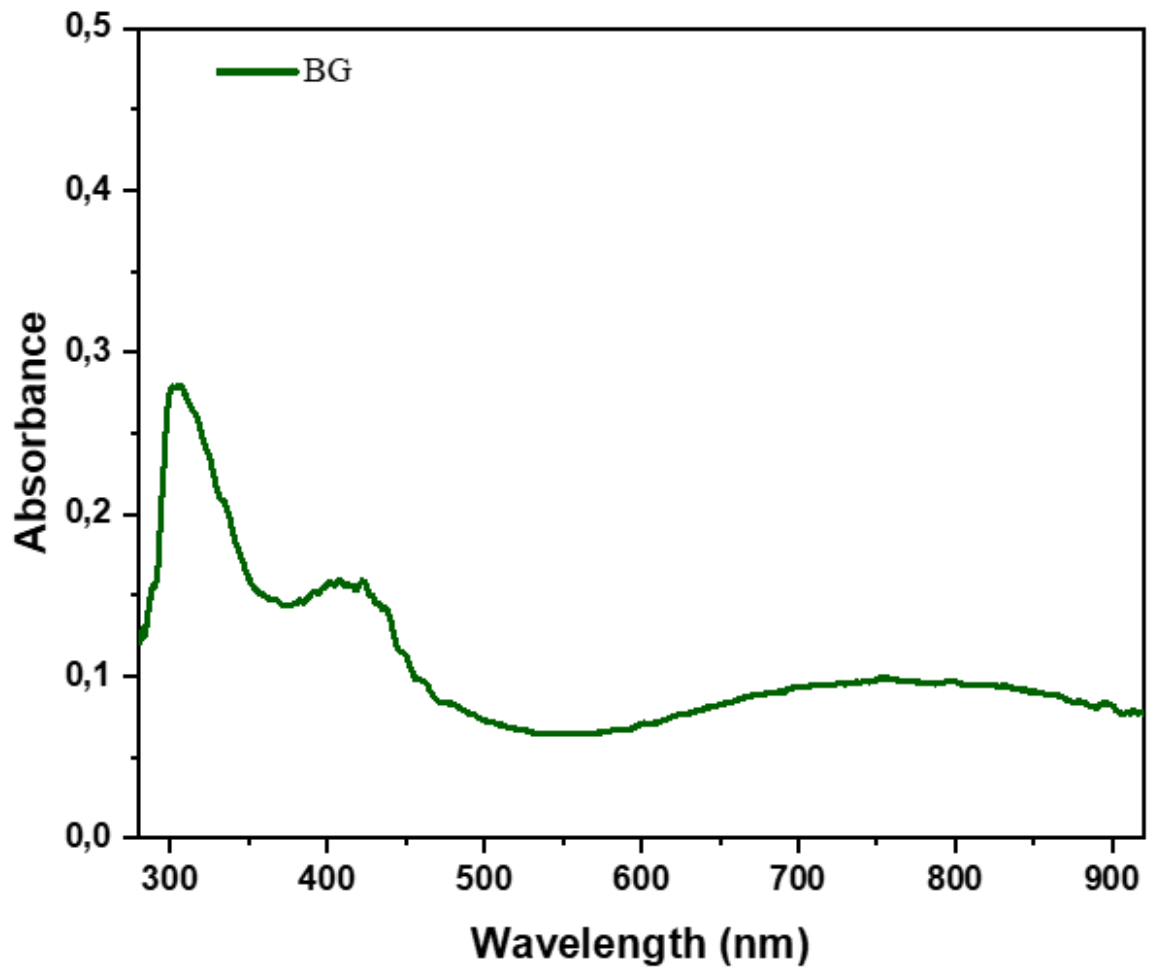


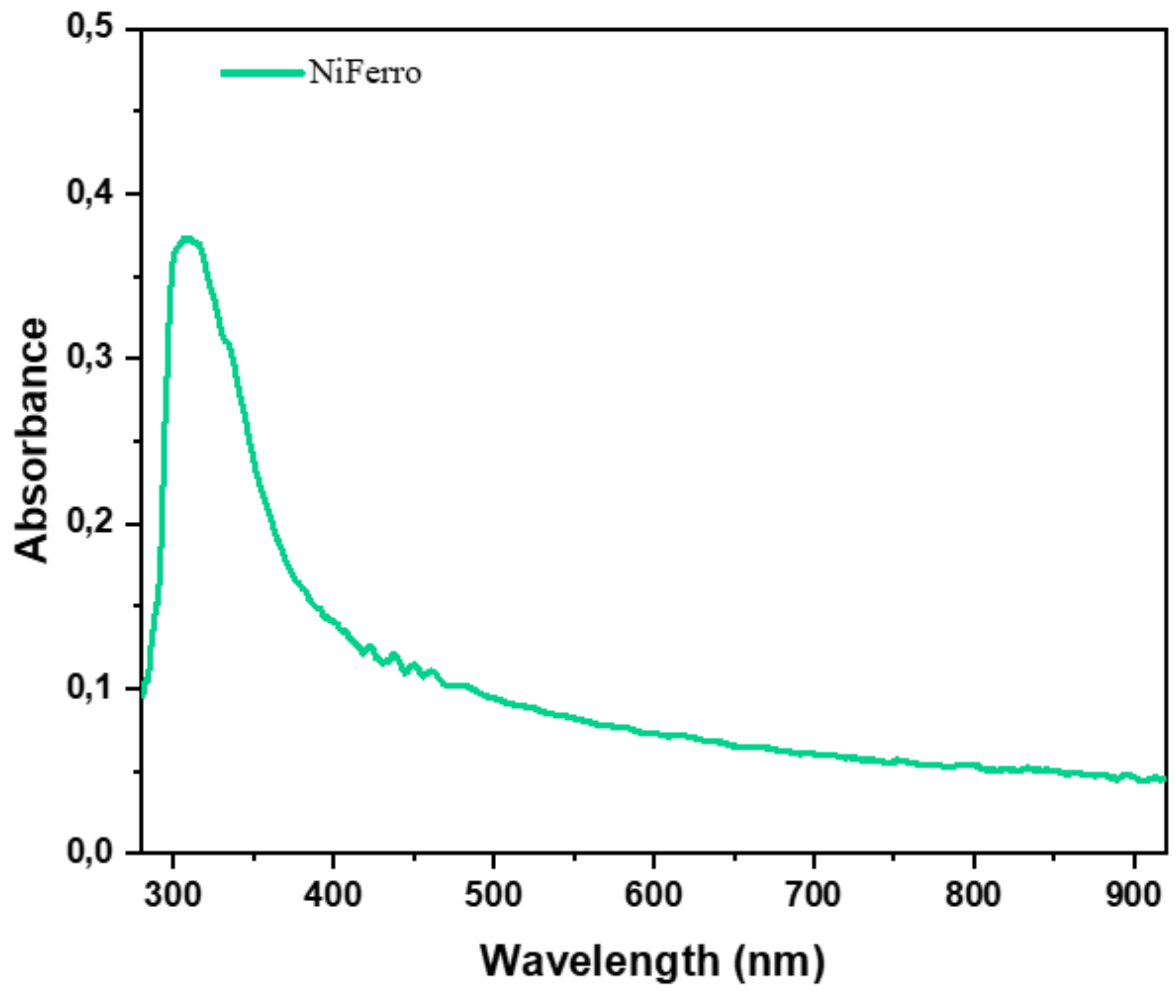
**S3:** Schematic oxygen quantification chamber during the electrocatalysis using a polarography dissolved oxygen sensor, and their respective quantification values using different working electrodes

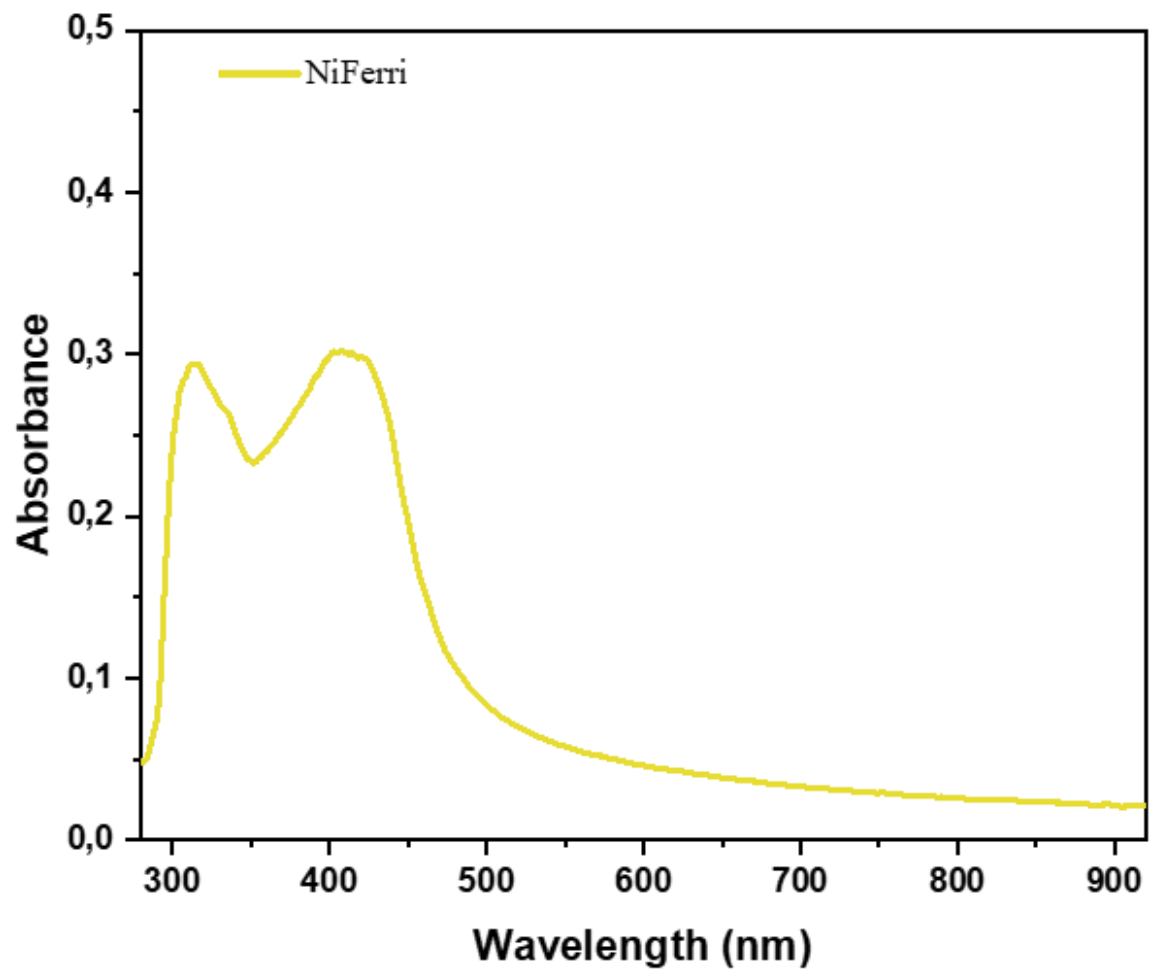




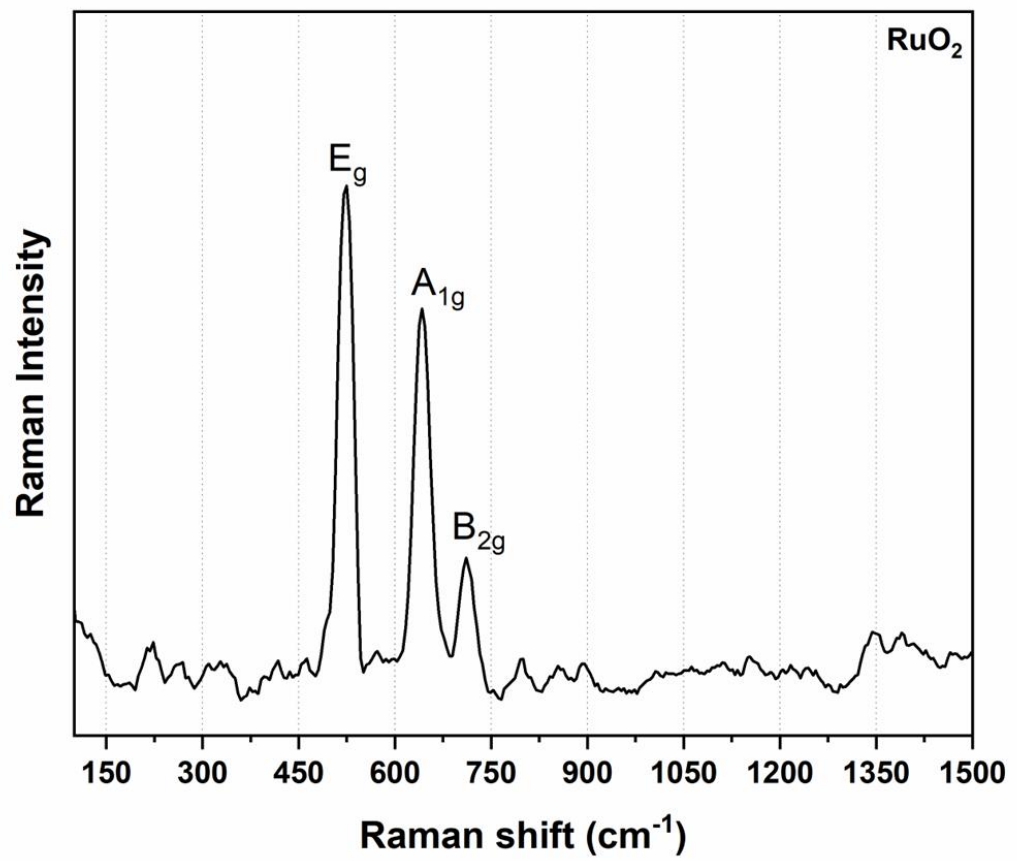




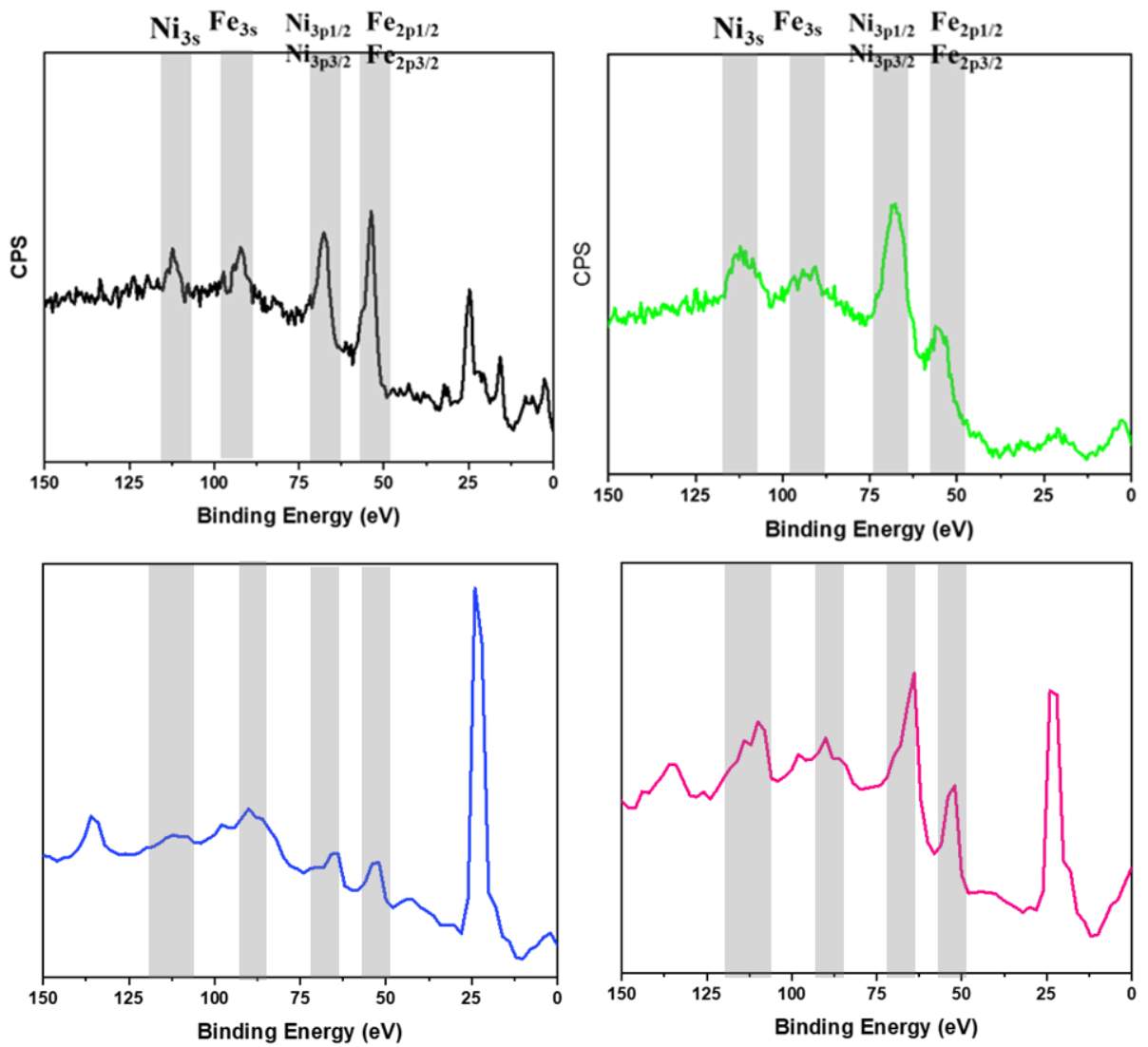




S4: UV-visible electronic absorbance spectra of  $\text{NiCl}_6 \cdot \text{H}_2\text{O}$ , Ferricyanide, Ferrocyanide, Prussian Blue, Berlin green, NiHCF(using ferrocyanide) and NiHCF(using ferricyanide), respectively.



**S5:** Raman spectroscopy of RuO<sub>2</sub> produced for catalysis comparison. The three peaks, are vibrational modes characteristics for RuO<sub>2</sub>.



**S6:** Soft X-ray photoelectron spectroscopy survey in 150 – 0 eV for NiHCF, NiHCF-vac, NiFeOx and NiFeOx-vac, in black, green, blue and pink lines, respectively. All these materials have slight differences in Ni 3s (111.0 eV), Fe 3s (91.3 eV), Ni 3p (67.5 – 66 eV) and Fe 3p (57.7 eV). Other peaks are assigned for FTO glass substrate.